Cell monolayers sense curvature by exploiting active mechanics and nuclear mechanoadaptation

Large-scale curvature sensing by epithelial monolayers depends on active cell mechanics and nuclear mechanoadaptation

Marine Luciano,[1#] Shi-Lei Xue,[2#] Winnok H. De Vos,[3] Lorena Redondo Morata,[4] Mathieu Surin,[5] Frank Lafont,[4] Edouard Hannezo,[2*] Sylvain Gabriele[1*]

[1] Mechanobiology & Soft Matter group, Interfaces and Complex Fluids Laboratory, Research Institute for Biosciences, CIRMAP, University of Mons, Place du Parc, 20 B-7000 Mons, Belgium

[2] Institute for Science and Technology Austria. Am Campus 1, A-3400 Klosterneuburg, Austria

[3] Laboratory of Cell Biology and Histology, Department Pharmaceutical, Biomedical and Veterinary Sciences, University of Antwerp, Antwerp, Belgium

[4] Cellular Microbiology and Physics of Infection Group, Center for Infection and Immunity of Lille, CNRS UMR 9017, INSERM U1019, CHU Lille, Institut Pasteur de Lille, University of Lille, F-59000 Lille, France

[5] Laboratory for Chemistry of Novel Materials, Research Institute for Biosciences, CIRMAP, University of Mons, Place du Parc, 20 B-7000 Mons, Belgium

[#]Contributed equally to this work

*To whom correspondence should be addressed: edouard.hannezo@ist.ac.at and sylvain.gabriele@umons.ac.be

Abstract

While many tissues fold *in vivo* in a highly reproducible and robust way, epithelial folds remain difficult to reproduce *in vitro*, so that the effects and underlying mechanisms of local curvature on the epithelial tissue remain unclear. Here, we photoreticulated polyacrylamide hydrogels through an optical photomask to create corrugated hydrogels with isotropic wavy patterns, allowing us to study how concave and convex curvatures affect cellular and nuclear shape. We find that the substrate curvature leads to thicker epithelial zones in the valleys and thinner ones on the crest, a feature which we show generically arises in vertex models, leading us to hypothesize that curvature-sensing could arise from resulting thickness modulations. We further show that concave and convex local curvatures lead to significant modulations of the nuclear morphology and positioning, a feature well-explained by an extension of vertex models taking into account membrane-nucleus interactions, where thickness modulation generically translate into corresponding changes in nuclear aspect ratio and position. Consequently, we find that the spatial distribution of Yes associated proteins (YAP), the main transcriptional effector of the Hippo signaling pathway, is modulated in folded epithelial tissues according to resulting nuclear density changes. Finally, we showed that these deformations are also associated with variations in the relative abundance of A/C- versus B1-type lamins, significant chromatin condensation and lower cell proliferation rate. These findings show that active cell mechanics and nuclear mechanoadaptation are key players of the mechanistic regulation of epithelial monolayers to substrate curvature, with potential application for a number of *in vivo* situations.

Introduction

In living systems, epithelial tissues are commonly described by three-dimensional (3D) microstructures such as invaginations, folds or wavy morphologies. Curved surfaces are also observed at interfaces between tissues or at boundaries between tissues and body lumen. The geometric form and biological function of wavy epithelial tissues are inherently linked together at all scales. For instance, crypts and villi of the small intestine provide a large surface area for exchange, improving the absorbance function. Despite its wide interest, the relationship between curvature and biological function in epithelial tissues remains largely unexplored [1,2].

Despite numerous studies on the influence of cellular and subcellular-scale topography on cell fate [3–5], few studies have investigated the effect of curvature on collective cell behavior [6–9], in particular because of the technical limitations encountered to engineer soft culture substrates with curved patterns in a controlled way [10]. It remains unclear in particular whether and how curvatures at scales much larger than cell size could be sensed biologically. Early studies conducted on glass fibers have shown that cells orient themselves along the line of minimal curvature to minimize cytoskeletal deformations [11,12]. Glass wires were also used to decouple the effect of out-of-plane curvature from the lateral confinement experienced during the migration of epithelial tissues [13]. More recently, it was shown that isolate adherent cells avoid crests of ultra-smooth sinusoidal surfaces during their migration and position themselves in valleys [14] and that the persistence and speed of migration of single cells can be affected by substrate curvature [15].

Despite these efforts, our current understanding of the role of the curvature of epithelial tissues remains elusive. To answer this question, we developed well-defined soft corrugated hydrogels to investigate the response of epithelial tissues to variations of curvature. By combining *in vitro* experiments with analytical and computational vertex

model, we show that local changes of monolayer thickness and cell density can be interpreted by energy minimization arising from the mechanics of apico-lateral tensions. We extended the vertex model to consider in a minimal way changes of nuclear morphology due to active tensions and cell shape, suggesting a simple mechanism via which thickness modulation couple to the experimentally observed changes in nuclear shape and positioning. We then showed that these changes triggered by curvature also lead to high nuclear/cytoplasmic YAP ratios, demonstrating a YAP-curvature sensing of epithelial tissues, which is inhibited at high cell density. Furthermore, we showed that nuclear deformations observed on corrugated matrices were associated with a modulation of lamin A/C (LMAC) and B1 (LMB1), leading to a lower expression of LMAC on positive curvatures and a higher expression of LMB1 on negative curvatures. Finally, we demonstrate that matrix curvature can be considered as an important regulatory cue of epithelial tissues, leading to high level of chromatin compaction and a lower DNA synthesis rate in negative curvature zones, which correspond to high cell density.

Results

The overall cytoskeletal architecture of wavy epithelial monolayers is not affected by the curvature.

To study how a monolayer of epithelial cells adapt to convex and concave cell-scale curvatures of their matrix (Fig. 1A), we generated corrugated hydroxypolyacrylamide (hydroxyPAAm) hydrogels by photopolymerizing an hydroxyPAAm solution at 360 nm through a chromium optical photomask. The polymerization was completed in transparent zones and the slow diffusion of the photoinitiator towards non-illuminated zones lead to the formation of a smooth and wavy profile. We used various widths of transparent and black

stripes to form isotropic corrugated hydrogels of 250±30 kPa with wavelengths of 20 μm (λ20), 30 μm (λ30) and 50 μm (λ50). We obtained symmetric corrugation patterns that formed wavy epithelial monolayers showing periodic wavelengths of 20 μm (Supplementary Movie S1), 30 μm (Supplementary Movie S2), 50 μm (Supplementary Movie S3) and constant amplitudes over large areas (10×10 mm^2).

To determine whether curvature changes can affect epithelial thickness and nuclear organization (Fig. 1A), we defined 3 zones of interest, as crests, valleys and interm. zones. Convex (positive) curvature zones correspond to the crests, concave (negative) curvature zones to the valleys and zero curvature zones to the interm., which corresponded to the junction between convex and concave zones (Extended Data Fig. 1A-B). We determined local maximal curvature values, amplitude (β) and wavelengths (λ) of convex and concave curvature zones using 2D (*xz*) profiles obtained from atomic force microscopy and high-resolution confocal microscopy (Extended Data Fig. 1A-C and Extended Data Table 1).

Corrugated hydrogels were functionalized with human fibronectin (FN) and Madin-Darby Canine Kidney (MDCK) cells were cultured at confluency (1×10^3 cells/mm^2) on flat hydrogels, λ20, λ30 and λ50 corrugated hydrogels for studying how convex and concave cell-scale curvatures can affect epithelial monolayers. After 48 hours in culture, wavy epithelial monolayers were immunostained with Alexafluor 488 for F-actin (Fig. 1B), 4′,6-diamidino-2-phenylindole (DAPI) for the nucleus (Fig. 1C) and imaged with a laser-scanning confocal microscope. Using Z-stack projections from confocal scanning of F-actin (Extended Data Fig. 2A-C), we found that the actin intensity was not significantly different between flat and corrugated (λ20, λ30 and λ50) hydrogels monolayers (Extended Data Fig. 2D, suggesting that corrugations of the matrix do not affect the global amount of F-actin in epithelia. We next studied the organization of cell-cell adhesive interactions in folded epithelial tissues by staining for ß-catenin, which is involved in regulation and coordination of MDCK cell-cell

adhesions[16]. ß-catenin staining showed that epithelial tissues remained cohesive on corrugated hydrogels (Extended Data Fig. 3A-C) with well-defined cell-cell contacts between polyhedral cells, independently of local concave or convex curvatures. We skeletonized ß-catenin stained images (Extended Data Fig. 3D-F) to determine a mean cell area of 205.3 ± 22.8 μm^2 on flat, 196.7 ± 27.7 μm^2 on λ20, 183.8 ± 17.8 μm^2 on λ30 and 186.8 8 ± 30.7 μm^2 on λ50 (Extended Data Fig. 3G), suggesting that corrugations did not change the mean cell area. Furthermore, we found that epithelial cells were characterized by a mean side number of 5.5±1.7 on flat, 5.8±1.3 on λ20, 5.8±1.3 on λ30 and 5.8±1.3 on λ50 (Extended Data Fig. 3H) and that the mean cell area increased with the polygon class (Extended Data Fig. 3I), regardless the corrugation wavelength.

Altogether, these results demonstrate that wavy epithelial monolayers maintain their overall architecture intact and can adapt to corrugated matrices without changing the mean cell shape nor the global expression of actin.

Epithelial thickness modulation from substrate curvature.

However, when examining the shape of the cell monolayer as a function of curvature (Fig. 1A), we found striking differences between convex zones (i.e. crests) and concave zones (i.e. valleys). In λ20, λ30 and λ50 tissues, cells on crests displayed reduced cell height and increased cell area (squamous-like), while cells in valleys were thicker and denser (columnar-like). Interestingly, similar density differences were observed in human keratinocytes [4], arguing this could be a general response to curvature. Given that a number of mechano-sensitive cellular responses, such as YAP localization, depend on cell thickness/density [17,18] as well as curvature [3], we thus hypothesized that curvature could be sensed indirectly by creating thickness/density differences, and turned to a theoretical model to understand how curvature could create such cell shape modulations.

For this, we used a vertex model [19–23], which describes the shape of epithelial monolayers based on their apical, lateral and basal tensions [24,25]. We first reduced the problem to 2D by neglecting the in-plane component that is translationally invariant, and assumed that the basal surface could not detach from the substrate [26] (with profile $\beta\cos(qx)$ where β is the amplitude of the substrate and q the wavevector), thus removing its contribution to the energy. Importantly, apart from measurable geometrical quantities such as cell density or volume, we found that the response of the monolayer to substrate curvature depended on a single rescaled parameter, the ratio of apical to lateral tensions Γ_a/Γ_l (Fig. 1A). Indeed, when apical tensions dominate, the configuration with minimum energy is the one with flat apical surface (leading to maximal thickness modulation, equal to substrate height modulation). However, this "flat-apical" configuration increases drastically total lateral area and is thus unfavorable for large lateral tensions. In that converse case, the epithelium tends to be of constant thickness, independent of curvature. In general, denoting $\alpha\cos(qx)$ the equation for the apical surface, the rescaled thickness modulation $\Omega = -(\alpha - \beta)/\beta$ is thus predicted to follow the law:

$$\Omega = \frac{\frac{1\Gamma_a}{2\Gamma_l}V_c q^2 - \frac{1}{4}\Delta h^2 q^2}{1+\frac{1\Gamma_a}{2\Gamma_l}V_c q^2 - \frac{1}{8}\Delta h^2 q^2} \quad (1)$$

which interestingly is independent of substrate amplitude β, allowing for simpler investigation of the specific effect of different substrate wavelengths (V_c is the cell volume and Δh the average thickness, see Supplementary Theory Note for details). We checked this analytical theory via numerical simulations of the 2D vertex model (on a fixed basal substrate) by varying multiple parameters such as wavelength, amplitude, tensions, and found that Eq. (1) matched well with numerical simulations at large wavelength, with small-wavelength corrections (Fig. 2A and Extended Data Fig. 4A-E).

Turning back to the data, we quantified this effect by projecting tissues along the direction of the pattern, thus building average intensity profiles in response to a curved substrate in each sample, from which we could extract the average basal and apical surfaces (Fig. 2B), and thus calculate Ω. Importantly, we found that thickness modulations Ω were largest for λ20 and smallest for λ50, as predicted theoretically (Fig. 2C). More quantitatively, the model could predict well the experimentally observed shape of the apical surface (Fig. 2D), and the evolution of the thickness modulation Ω across wavelength (λ20, λ30 and λ50) was well-predicted by Eq. (1) with the single fitting parameter $\frac{\Gamma_a}{\Gamma_l} = 0.6 \pm 0.2$ (with all other parameters, such as cell seeding density, substrate deformation amplitude β, average cell thickness, being constrained from independent measurements, see Supplementary Note for details). Interestingly, even for substrate with strongly non-symmetric profiles (e.g. the substrate with larger wavelength of 100 μm in Extended Data Fig. 5A), although the analytical Eq.1 could not readily be applied, we found that vertex model simulations (taking this more complex substrate shape as an input, with all other parameters kept the same as λ20, λ30 and λ50) still gave good agreement with the experimental shape profile (Extended Data Fig. 5B). Furthermore, one important prediction of the theoretical model is that the rescaled thickness modulation $\Omega = -(\alpha - \beta)/\beta$ does not change with substrate amplitudes, i.e. doubling the substrate amplitude doubles the absolute thickness modulation (so that the ratio of the two does not change). To further test this prediction, we varied the amplitudes of corrugated hydrogels of 20 μm and 50 μm wavelength, so they both have substrate amplitudes either distinct from or close to a fixed amplitude of ~2.3 μm (i.e. the amplitude of 30 μm wavelength substrates) (Extended Data Fig. 5C and Extended Data Table 1). We were therefore able to compare the thickness modulation of varied substrate wavelengths (20, 30 and 50 μm) with a fixed amplitude or varied substrate amplitude with the same wavelength. Importantly, we found no statistically significant differences when comparing the normalized

thickness modulation (Ω) of λ20/1.2 with λ20/2.3 and λ50/2.4 with λ50/3.2 (Extended Data Fig. 5D). This confirmed our model prediction, where amplitude changes have a linear effect on thickness modulation (resulting in an invariance rescaled thickness modulation) and allow us to compare rescaled thickness modulations for different wavelengths (as previous analysis of Fig. 2C).

Altogether, the theory suggests that active contractile apico-lateral tensions could be a very simple physical mechanism converting changes in substrate curvature into changes in cellular thickness/densities.

Substrate curvature modulates the spatial distribution of nuclei.

Next, we asked whether modulation of epithelial thickness in response to substrate curvature changes would impact the spatial distribution of nuclei. To answer this question, we extended our vertex model to consider the mechanical interaction between the nucleus (modelled as a deformable sphere under tension) and cell surfaces (Extended Data Fig. 4F for sketch, see Supplementary Theory Note for details). Intuitively, apical surface in convex zones (with thin monolayer) were expected to compress nuclei in-plane, whereas apical surface in concave zones (with thick monolayer) were expected to compress nuclei along the apico-basal axis (Extended Data Fig. 4G-I see also Supplementary Theory Note for analytical expressions). Furthermore, in the presence of cell thickness gradient (which arises generically from thickness modulation), nuclei are expected to move along the thickness gradient towards large thicknesses to minimize nuclear deformation, and we predicted a linear relationship between thickness gradient and nuclear displacement away from the cell center of mass (Extended data Fig. 4I and Supplementary Theory Note).

Interestingly, clear differences between nuclear and cellular centers of mass in corrugated epithelia were observed on confocal images (Fig. 3A), suggesting that nuclei were

attracted from intermediate zones to concave ones (valleys). We therefore defined a vector between two centers of mass representing "nuclear offset" (Fig. 3A-B), as a function of normalized position $\bar{x} = \frac{x}{\lambda}$ ($\bar{x}$=0 and 1 corresponded to the convex regions and $\bar{x}$=0.5 to the concave region). To test whether the vertex model can predict these changes of nuclear localization, we computed in both model and data the nuclear offset and confirmed that the experimental data also followed a sinusoidal dependency with position *x* for all wavelengths. As predicted by the model, nuclear offset was directed towards concave zones (i.e. valleys), away from convex ones (i.e. crests), and maximal on the intermediate zones (Fig. 3C). Importantly, the amplitude of the sinusoidal of the offset depended on one fitting parameter (quantifying the relative nuclear/surface tensions, see Supplementary Theory Note for details), which allowed us to jointly fit the λ30 and λ50 data (as expected, λ50 showed lower amplitude than λ30).

One discrepancy was that the continuum model predicted that λ20 should have an even larger offset than λ30, while the opposite was found in experiments (Fig. 3C). However, turning to discrete vertex model simulations, we found that this was expected when considering such small wavelengths. Indeed, for small wavelengths (i.e. on order of cellular size), we found that numerical simulations generically predicted a "quantization" of the nuclear response with substrate wavelength, i.e. when the substrate wavelength represents integer values of cell lengths (Fig. 3D-G). For instance, for 2 cells per wavelength (close to the λ30 scenario, Figs. 3F,G), the energy minimum of the vertex model is to have each cell spanning half-a-period between one valley and one crest, maximizing the thickness gradient and allowing nearly full localization of nuclei in concave zones (valleys). This cannot occur for non-integer values (Fig. 3D), which can occur for λ20 substrates (Fig. 3E, see Supplementary Theory Note for more detailed discussion), explaining the lower nuclear offset compared to λ30 in this condition. We also tested whether other features of the model, such as

the curvature-dependent nuclear deformation observed in data and found that nuclear projected area (Extended data Fig. 6A) followed closely the theoretical prediction of a sinusoidal dependency as a function of *x*, with largest (resp smallest) projected nuclear area (*xy* plane) in convex (resp. concave) regions for all wavelengths (Extended Data Fig. 6C-E), i.e. the spatial dependency of projected area was similar to offset, but with a 90° phase difference (see Supplementary Theory Note for details). Altogether, these quantitative analyses strengthen the mechanism we propose where thinner convex zones compress nuclei in-plane, whereas thicker concave zones compress nuclei along the apico-basal axis.

Based on this finding, we also examine the third dimension (*y*-direction), along the corrugations, and found that the corrugation dimension modulated the orientation of nuclei. Interestingly, our results showed that the nuclei densely accumulated in the concave zones (i.e. valleys, Extended Data Fig. 6B) were significantly more likely to align along *y*-axis (Extended Data Fig. 1A), with angle of orientation 15.8±6.2° on λ30 (Extended Data Fig. 7A), whereas nuclei formed a wider orientation distribution on convex regions (i.e. crest), with angle 49.9±17.1° on λ30 (Extended Data Fig. 7B).

Altogether, the combined quantitative analyses and experimental measurements reveal that epithelial thickness modulation due to substrate curvature can affect nuclear positioning and deformation. In the following, we further explore the accompanying nuclear biochemical changes arising from curvotaxis.

YAP-curvature sensing is mediated by nuclear density modulation.

Recent works have demonstrated that direct application of forces to the nucleus was sufficient to regulate the activity of YAP, a central regulator of cell proliferation and fate, by controlling its transport through nuclear pores [27–29], as well as a number of nuclear mechano-transduction events being increasingly recognized [30,31]. Given the nuclear positioning and

morphological changes we observed, we take a closer look at how YAP localization is affected by curvature. Interestingly, YAP is well-established to adapt its nuclear-cytoplasmic localization as a function of cellular density [18], but has also been shown to be dependent on substrate curvature via unknown mechanisms [4]. Given our findings that curvature generically translates into cellular density changes (as well as nuclear density changes reinforced by nuclear offset), we thus propose a hypothesis that the curvature sensing of YAP could be a consequence of the nuclear density modulation.

To examine the impact of substrate corrugations on YAP translocation, epithelia were grown at 1×10^3 cells/mm^2 on flat, λ20, λ30 and λ50 wavy hydrogels and immunolabeled after 48h for YAP and DNA (Fig. 4A). We performed high magnification confocal imaging experiments to quantify the nuclear/cytoplasmic YAP ratio in epithelial cells located on convex, interm. and concave zones. Our results showed that the nuclear/cytoplasmic YAP ratio increased on convex (crest) curvatures but decreased on concave (valleys) ones (Fig. 4B and Extended Data Fig. 7C-E). At constant curvature, we found that the nuclear/cytoplasmic YAP ratio was larger on convex (2.45±0.47 for C=0.27 on λ30) than on concave (2.00±0.38 for C=-0.27 on λ30) curvature zones (Fig. 4A), as predicted from the decreased cellular density there (Extended Data Fig. 6B). Our results are thus consistent with the hypothesis that YAP curvature-sensing could occur indirectly from density-sensing. To test this further, we reasoned that YAP curvature-sensing should then be absent for higher overall densities, as in the model density then becomes high even in crests and overall rescaled thickness modulations are reduced (see Supplementary Theory Note and Extended Data Fig. 4A).

We thus studied very dense epithelial tissues (5×10^4 cells/mm^2) on flat, λ20, λ30 and λ50 hydrogels [32,33], and found a low (<1) nuclear/cytoplasmic YAP ratio, which was unaffected by the substrate curvature (Fig. 4C), confirming that high cell density can inhibit YAP curvature-sensing from epithelial cells. Furthermore, superimposing the mean

nuclear/cytoplasmic YAP ratio on flat, λ20, λ30 and λ50 substrates versus the local nuclear density (concave and convex zones) confirmed the hypothesis that YAP curvature-sensing could occur indirectly from density-sensing (Fig. 4D).

Finally, we sought to apply our theory to previously published dataset on keratocytes, and found that we could again explain multiple features of these within our theory (with larger apical/lateral tension ratio $\Gamma_a/\Gamma_l=5$, see Supplementary Note and Extended Data Fig. 4D), including the magnitude of valley/crest density differences, and the delamination of cells from the crests above a critical value of substrate curvature (see Extended Data Fig. 4D and Supplementary Theory Note for details). This argues for a generality of such a mechanism of density/thickness changes from curvature, with impact on YAP.

Substrate curvature modulates the relative abundance of nuclear lamina.

Given our findings that substrate curvature leads to differential nuclear deformations, we sought to evaluate the lamina composition in deformed nuclei, as a potential mechano-sensitive response [34]. Indeed, accumulating evidence shows that the nuclear mechanical properties are viscoelastic [35] and controlled the stoichiometric ratio between B1-type (LMB1) and A/C-type (LMAC) lamins [36,37,38]. By scanning confocal microscopy, we examined the fluorescence intensity of A/C-type (TRITC in red) and B1-type (FITC in green) lamins on convex, interm. and concave zones of λ20 corrugated hydrogels (Fig. 5A). Z-stack images using a ×60 objective were collected for three channels (DAPI, TRITC and FITC) from the entire volume of the nuclei using a step size of 0.15 μm. Exposure times and laser power were kept constant and acquired stack of images was deconvolved to remove out of focus light.

Using Z-stack images of nuclei located on convex (Supplementary Movies S4 and S5), interm. (Supplementary Movies S6 and S7) and concave (Supplementary Movies S8 and S9) zones (Fig. 5B), we estimated the mean integrated density of DAPI, LMAC and LMB1

(Fig. 5C) for each Z-plane and calculated the LMAC/LMB1 integrated density ratio to characterize the relative abundance of A/C- versus B1-type lamins. For each nuclear morphology, we defined three Z planes of interest: Z_0 (basal plane), Z_1 (mid plane) and Z_2 (apical plane), respectively at 15%, 50% as 85% of the total nuclear height (Fig. 5B). The mean integrated densities of DAPI, LMAC and LMB1 versus the nuclear height for the three nuclear morphologies (n=8 for each with N=3 replicates) were characterized by Gaussian-like distributions. The LMAC/LMB1 ratio for convex zone was slightly below 1 for the apical part (Z_0, Fig. 5D) and close to 1 for $Z>Z_1$, indicating that the LMA abundance was lower on convex curvatures. For nuclei in interm. zones, the LMAC/LMB1 ratio was ~1.7 at Z_0, then decreased abruptly to Z_1 to reach a value of ~0.5 for $Z_1<Z<Z_2$. The asymmetric nuclear shape on interm. zones were characterized by more LMB1 in the apical part ($Z_1<Z<Z_2$) and more LMAC in the basal one ($Z_0<Z<Z_1$). Interestingly, the relative abundance of LMAC was significantly higher for nuclei in the concave zones, with maximal values at Z_0 (basal) and Z_2 (apical) focal planes (Fig. 5D).

Taken together, our results indicated that the nuclear deformations lead to a higher abundance of B1-type lamins on convex curvatures (i.e. crests) and a higher abundance of A/C-type lamins on concave curvatures (i.e. valleys), suggesting that the nuclear deformations induced by substrate curvature changes are accompanied by significant modulations of both A-type and B-type lamins (Fig. 5E).

Concave curvatures lead to lower cell proliferation rate and promote significant chromatin condensation.

Finally, the modulation of nuclear shape, YAP localization and the relative abundance of A/C versus B1 lamins by substrate curvature led us to question how matrix corrugations affect cell functions, such as proliferation and DNA synthesis. To answer this question, we

sought to test whether our vertex 2D model can be extended to predict some functional changes in deformed nuclei. We therefore extended our 2D mechanical model of the nucleus to 3D to further explore how stresses arising from curvature could modulate 3D nuclear deformations and volume. We did so by a combination of analytical arguments and 3D finite element simulations from a minimal model of nuclear mechanics (see Supplementary Note for details). We first considered the simplest case of nuclei compressed into flat shapes (Fig. 6A), as observed on crests. As shown in Fig. 6B, the model predicted that increasing the amount of compression from the apical surface of the monolayer also generically decreases nuclear volume. Similarly, nuclei in valleys are predicted to be deformed due to the "offset" forces, thus also decreasing their volume (see Supplementary Theory Note for details). To test both theoretical predictions, we examined whether nuclear volume was affected by curvature, using high magnification confocal Z-stacks of nuclei located on convex, interm. and concave zones of λ20 (Fig. 6C) and λ30 (Fig. 6D) corrugated hydrogels. Cells on convex and concave zones of λ20 and λ30 hydrogels exhibited lower nuclear volumes than those on interm. zones, suggesting that both convex and concave curvatures decreased nuclear volumes. Interestingly, lowest nuclear volumes were found in cells located on concave zones (i.e. valleys) of λ20 (635 ± 233 μm^3) and λ30 (776 ± 116 μm^3), demonstrating that prolate nuclear shapes and high nuclear densities in concave zones resulted in a significant nuclear volume loss.

Secondly, we checked whether substrate curvature can affect chromatin organization, using a quantitative procedure based on DAPI staining [39,40]. Indeed, the uptake of DAPI depends on the total amount of DNA, but also on its level of condensation [41]. The average spatial density corresponding to the ratio between the integrated fluorescence intensity and the volume of the nucleus is therefore a reliable indicator of the *in-situ* average chromatin condensation. As shown in Figs 6E-F, marked reorganization of chromatin distribution was associated with nuclear deformations in concave zones of λ20 and λ30 corrugated hydrogels.

Highly condensed chromatin domains showed higher fluorescence intensity with respect to the less condensed ones. The quantification of the chromatin to nuclear ratio indicated that nuclei deformed in concave zones of λ20 (Fig. 6G) and λ30 (Fig. 6H) showed the highest chromatin compaction values with 0.27±0.03 and 0.37±0.16, respectively. Our results indicated therefore that prolate nuclear shapes in concave curvature zones were associated with a high level of chromatin compaction that may affect DNA synthesis.

To test this hypothesis, we used the incorporation of a thymidine analog, 5-ethynyl-2′-deoxyuridine (EdU), as a proliferation marker. A 24-hour incubation period was chosen because it allowed EdU incorporation on corrugated and flat hydrogels, without no saturation of EdU incorporation in MDCK cells. The Edu-positive ratio was calculated as the ratio between Edu and Hoechst-stained cells in a particular field of view (Fig. 6I). We observed lower rates of positive-EdU nuclei on convex curvatures of λ20 (0.31±0.08) and λ30 (0.32±0.07) than on flat hydrogels (0.42±0.05), regardless the positive curvature value (Fig. 6H). Furthermore, our findings showed that the rate of positive-EdU nuclei in concave zones was roughly divided by a factor two with 0.18±0.06 on λ20 and 0.25±0.11 on λ30, demonstrating that the DNA synthesis was significantly decreased in elongated cells accumulated in concave curvature zones.

Taken together, these results indicated that concave curvature zones of corrugated matrices were characterized by a high density of prolate-shaped nuclei, which were associated with a high level of chromatin compaction and a lower DNA synthesis rate.

Discussion

The role of the substrate curvature has been mainly described so far at the single-cell level, establishing that cells orient themselves along the line of minimal curvature to minimize cytoskeletal deformations. Here, we explore the hypothesis that confluent epithelial

monolayers can also sense large-scale curvature via active cell mechanics and nuclear mechano-sensing. Our findings reveal that substrate curvature leads to thicker epithelial zones in concave zones (i.e. valleys) and thinner ones on convex zones (i.e. crests), as well as corresponding cellular densities. This is fully recapitulated in a physical model of apico-lateral active tension, where thickness modulation arises generically as stable states of the monolayer (and consistent with findings of a pre-print released during the preparation of this manuscript [42]), leading us to hypothesize that matrix curvature sensing could arise from resulting density/thickness changes. Furthermore, we develop a minimal theory for how thickness modulations imposed by the substrate can impact nuclear morphometrics, such as nuclear deformation, aspect ratio and positioning relative to the local curvature. These predicted flattened nuclei on convex curvature zones, but also a movement of nuclei towards the concave zones in order to minimize their deformation in response to thickness gradients. We verified these features in experiments, including non-trivial features such as enhanced responses to specific wavelengths. Together, these findings show that physical processes allow epithelial monolayers to respond to curvature changes, leading to the appearance of different types of nuclear deformations and orientations.

Given accumulating evidence of nuclear mechano-transduction processes [31,43–46] we then investigated how these physical changes translated into mechano-responses and biochemical changes within the cells as a function of local curvature. We showed that the patterns of cellular densities generated by the matrix curvature are associated with significant changes in the spatial distribution of YAP [3,4], consistent with the idea of curvature-sensing occurring via physically-driven thickness/density-changes. YAP in particular has been shown to be is a key transcription factor that mediates the interplay between cellular mechanics and signaling cascades underlying gene expression, cell proliferation, differentiation fate decisions, and organ development. The spatio-temporal localization of YAP provides

417 therefore critical information about the regulatory state of the cell and in the future, it will be
418 interesting to probe the generality of these findings to other cellular lines and physiological
419 contexts.

420 In addition to YAP response, our results also indicated that lamin A/C versus B1 ratio
421 [47,48], chromatin condensation and cell proliferation rate are all modulated by substrate
422 curvature, demonstrating that substrate curvature sensing modulates multiple
423 mechanotransduction pathways in cell assemblies. The correlation of YAP and lamins with
424 stem cell differentiation and cell division has suggested recently a relationship between the
425 expression of both proteins in deformed nuclei [49], which would be a natural next step of
426 investigation. Our study therefore provides insights into the mechanistic regulation of
427 epithelial monolayers to large-scale substrate curvature, with potential impact for a large
428 number of physiological situations, given the ubiquitous presence of curvature *in vivo*.

429

430 **Materials and Methods**

431

432 **Fabrication of corrugated polyacrylamide hydrogels by UV-photocrosslinking**

433 Instead of the standard radical polymerization using catalysts such as tetramethylenediamine
434 (TEMED) and ammonium persulfate (APS), which lead to slow polymerization times, we
435 used an Irgacure 2959 photoinitiator (2-Hydroxy-4′-(2-hydroxyethoxy)-2-
436 methylpropiophenone) to polymerize hydroxypolyacrylamide (hydroxy-PAAm) hydrogels.
437 Hydroxy-polyacrylamide (hydroxy-PAAm) hydrogels were prepared by mixing acrylamide
438 (AAm), bis-acrylamide (bis-AAm), N-hydroxyethylacrylamide (HEA), 2-Hydroxy-4′-(2-
439 hydroxyethoxy)-2-methylpropiophenone (Irgacure 2959, Sigma #410896) and deionized
440 water. A solution composed of 2836 µL of acrylamide (AAm, Sigma #79-06-1) at 15% w/w
441 in deionized water, 1943 µl of N,N'- methylenebisacrylamide (BisAAm, Sigma #110-26-9) at

2% w/w in deionized water, and 1065 µL N-hydroxyethylacrylamide monomers at 65 mg/mL in deionized water (HEA, Sigma #924-42-5) were mixed together in a 15 mL Eppendorf tube [50–52] and deionized water was added to reach a final volume of 6 mL. We prepared a stock solution of Irgacure 2959 in sterile deionized water at 5 mg/mL. We introduced 1 mL of the stock solution into the 6 mL of the hydrogel solution [53] to obtain a final concentration of 0.7 mg/mL. After a gentle mixing, the solution was degassed during 30 min under a nitrogen flow. Glass coverslips of 22 mm^2 in diameter were cleaned with 0.1 M NaOH solution during 5 min and then rinsed abundantly with deionized water during 20 min under agitation. Cleaned glass coverslips were then treated during one hour with 3-(trimethoxysilyl)propyl acrylate (Sigma #2530-85-0) to promote a strong adhesion between the hydroxy-PAAm hydrogel and the glass coverslips and finally dried under a nitrogen flow. A volume of 40 µL of the degassed mixture was squeezed between an activated glass coverslip and a chromium optical photomask (Toppan photomask, France) and before exposition to UV illumination at 360 nm (Dymax UV light curing lamp). Chromium optical photomasks with alterning transparent stripes of 10 µm wide and black stripes of 10 µm or 20 µm wide were used to form corrugated hydrogels with wavelengths of 20 µm (λ20), 30 µm (λ30) and 50 µm (λ50) and respectively. After UV exposition at 360 nm during 10 min at 10 mW/cm^2 through the optical photomask, the polymerization was completed and a corrugated hydroxy-PAAm hydrogel was formed. The amplitude of 20 µm (λ20) and 30 µm (λ30) corrugated hydrogels was changed by adjusting the volume of the degassed polyacrylamide solution squeezed between the glass coverslip and the chromium optical photomask. Finally, hydrogels were gently removed from the photomask under water immersion, washed three times in sterile deionized water under gentle agitation and stored in sterile deionized water at 4°C. Photocrosslinked hydroxy-PAAm hydrogels were optically transparent and did not exhibit any autofluorescence background at 470±20 nm, 562±88 nm and 591±21 nm.

Characterization of corrugated hydrogels by atomic force microscopy

Atomic force microscopy (AFM) measurements were performed on dried and immersed photoreticulated hydrogels to characterize their corrugations [54,55]. AFM of dried hydrogels were performed at room temperature with an ICON instrument from Bruker using the Peak Force mode in order to minimize the applied force. AFM of swollen hydrogels were performed in PBS at 7.2 pH using a NanoWizard TM 3 AFM (JPK Instruments, Berlin, Germany) operated in Quantitative Imaging (QI) mode. Once the coverslip containing the gel was placed on the stage of the microscope, the cantilever was positioned far above the glass surface and allowed to thermally equilibrate during 30 min. Cantilevers were purchased from Bruker (MLCT-BIO-DC-F: k = 0.6 N/m, f = 125 kHz; silicon nitride; front angle 35 ± 2°; quadratic pyramid tip shape). Cantilever spring constant and sensitivity were calibrated before each experiment using the JPK software. The force trigger was adjusted to have a high indentation without damaging the gel. Tip velocity was maximized within instrument limits and ramp size was reduced with a short baseline in order to minimize the acquisition time. Data were analyzed with the NanoWizard® Data Processing software version 6.1.96 and the stiffness was calculated according the Hertzian contact model (Young's modulus), fitting the distribution to Gaussians. We obtained a Young's modulus of 250±30 kPa, which is close to the physiological situation and corresponds to the optimal window of elasticity required for vinculin assembly, actin fiber formation and, subsequently, to initiation of replication in kidney epithelial cells [56].

Cell culture

Epithelial cells from the Madin-Darby Canine Kidney cell line (MDCK II, Sigma #85011435) were maintained in polystyrene T75 flasks of in a cell culture incubator at 37°C and 5% CO_2.

MDCK cells were cultured in proliferation medium composed of Dubelcco's Modified Eagle's medium (DMEM), high glucose (4.5 g/l) with L-glutamine (BE12-604F, Lonza) supplemented with 10% (v/v) Fetal Bovine Serum (FBS, AE Scientific) and 1% of penicillin and streptomycin antibiotics (AE Scientific) [57,58]. MDCK cells were seeded on flat (control), λ20, λ30 and λ50 corrugated hydrogels at a density of 1.10^3 cells/mm^2 for 48 hours. YAP immunostained experiments were also performed at a higher cell density of 5.10^4 cells/mm^2. The cell density was estimated from the ratio of the mean number of nuclei to the surface area, which was corrected by considering the projection effect of λ20, λ30 and λ50 corrugated hydrogels.

Proliferation assays

The S-phase synthesis of the cell cycle was labeled in living epithelial tissues grown on corrugated hydrogels using the Click-iT EdU (5-ethynyl-2'-deoxyuridine) (Thermofischer Scientific, A20174) for 30 minutes in proliferation media. Proliferation of MDCK cells on corrugated hydrogels was assessed using the Click-iT EdU Alexa (647 or 555) kit (Thermofischer Scientific, C10338). Briefly, epithelial tissues were incubated with a 10 μM solution of EdU in complete medium for 30 min. Then, tissues were rinsed with PBS, fixed for 10 min with a 4% PFA solution and permeabilized for 20 min with a 0.5% solution of Triton X-100. MDCK tissues cells were blocked with 3% BSA and incubated for 30 min in the dark with a reaction cocktail composed of Click-iT reaction buffer, CuSO4, AlexaFluor azide and reaction buffer additive. MDCK tissues were rinsed with PBS three times and labelled with Hoechst 33342 before mounting in slow fade gold antifade.

Immunostaining of epithelial tissues

MDCK cells were fixed and permeabilized with 4% paraformaldehyde (Electron Microscopy Sciences), 0.05% Triton X-100 (Sigma) in phosphate buffered saline (PBS 1X, Capricorn scientific) for 12 min at room temperature. Fixed cells were rinsed three times in warm PBS and incubated 30 min with a blocking solution containing 1% BSA (Bovine Serum Albumine, GE Healthcare) and 5% FBS in PBS. MDCK cells were labeled for F-actin with Alexa Fluor 488 Phalloidin, 1:200, DNA with DAPI at 1:200 (ThermoFisher Scientific, #D1306) and ß-catenin [59]. Yap was labeled with YAP1 monoclonal antibody produced in mouse (Abnova, clone 2F12), ß-catenin with anti ß-catenin produced in mouse at 1:200 Sigma-Aldrich, #C2206) for 45 min at 37°C. MDCK cells were washed three times in PBS, incubated with an anti-mouse antibody produced in goat and labeled with a goat anti-mouse antibody at 1:200 (Molecular Probes, tetramethylrhodamine, Invitrogen, T2762) for 45 min at 37°C. Lamin B1 (LMB1) and Lamin A/C (LMAC) proteins were labelled with a polyclonal anti-lamin B1 antibody produced in rabbit (1:200, Abcam, ab16048) and a monoclonal anti-lamin A/C antibody produced in mouse (1:200, Santa Cruz Biotechnology, SC-376248), respectively. Epithelial tissues were incubated for 45 min at 37°C with both antibodies. Immunostained cells were mounted on microscope slides with slowfade gold antifade (Thermofisher, Molecular probes) for epifluorescence and confocal imaging.

Epifluorescence and confocal imaging

MDCK epithelial tissues were observed in epifluorescence and confocal mode with a Nikon A1R HD25 motorized inverted microscope equipped with x20, x40, x60, x100 Plan Apo (oil, NA=1.4 or silicon, NA=1.4) immersion objectives and lasers that span the violet (405 and 440 nanometers), blue (457, 477, and 488 nanometers), green (514 and 543 nanometers), yellow-orange (568 and 594 nanometers), and red (633 and 647 nanometers) spectral regions. Epifluorescence images were recorded with a photometrics Prime 95B camera (Photometrics

Tucson, AZ) using NIS Elements Advances Research 4.5 software (Nikon). Confocal images using small Z-depth increments (0.15 μm) were processed using NIS-Elements (Nikon, Advanced Research version 4.5). Photopolymerized (Irgacure 2959) hydroxy-PAAm hydrogels did not exhibit any autofluorescent signal at 470±20 nm (DAPI), 562±88 nm (FITC) and 591±21 nm (TRITC).

Morphometric analysis of the nuclei

The morphometric analysis of the nuclei was conducted using the trainable WeKa segmentation plugin for FIJI [60] that first calculates the barycenter, extracts contour, perimeter and projected area of each nuclei. Then the contour of each nuclei of 1 pixel in thickness was defined as a region of interest (ROI). By using the "exclude on edges" function of FIJI, we automatically exclude any ROI that have at least one pixel that overlaps the frame of the image from the working population of nuclei. Then the algorithm generates an ellipse to fit the nuclear contour and determine the orientation angle of each nuclei with respect to the orientation of the corrugations.

Statistical analysis

Differences in means between groups were evaluated by two-tailed Student's t-tests performed in Prism 9 (Graphpad Software, Inc.). For multiple comparisons the differences were determined by using an analysis of variance (ANOVA) followed by Tukey post-hoc test. *$p < 0.05$, **$p < 0.01$, ***$p < 0.001$, ****$p < 0.0001$ and n.s. not significant. Unless otherwise stated, all data are presented as mean ± standard deviation (S.D.).

Acknowledgments

S.G. acknowledges funding from FEDER Prostem Research Project no. 1510614 (Wallonia DG06), the F.R.S.-FNRS Epiforce Project no. T.0092.21 and the Interreg MAT(T)ISSE project, which is financially supported by Interreg France-Wallonie-Vlaanderen (Fonds Européen de Développement Régional, FEDER-ERDF). This project was supported by the European Research Council under the European Union's Horizon 2020 Research and Innovation Program Grant Agreements 851288 (to E.H), and by the Austrian Science Fund (FWF) (P 31639 to E.H.). L.R.-M. acknowledges funding from the Agence National de la Recherche (ANR), as part of the "Investments d'Avenir" Programme (I-SITE ULNE / ANR-16-IDEX-0004 ULNE). This work benefited from ANR-10-EQPX-04-01 and FEDER 12001407 grants to F.L. W.H.D.V. acknowledges FWO Grant number G005819N. M.L. is financially supported by FRIA (F.R.S.-FNRS). M.S. is senior research associate of the Fund for Scientific Research (F.R.S.-FNRS) and acknowledges the grant EOS No. 30650939 (PRECISION). Stably transfected m-cherry E-cadherin MDCK was kindly provided by Benoît Ladoux. Sketches in Fig. 1A, Fig. 5E and Extended Data Fig. 9 were drawn by Carolina Levicek.

References

1. Baptista, D., Teixeira, L., van Blitterswijk, C., Giselbrecht, S. & Truckenmüller, R. Overlooked? Underestimated? Effects of Substrate Curvature on Cell Behavior. *Trends in Biotechnology* **37**, 838–854 (2019).
2. Altay, G., Tosi, S., García-Díaz, M. & Martínez, E. Imaging the Cell Morphological Response to 3D Topography and Curvature in Engineered Intestinal Tissues. *Front. Bioeng. Biotechnol.* **8**, 294 (2020).
3. Walko, G. *et al.* A genome-wide screen identifies YAP/WBP2 interplay conferring growth advantage on human epidermal stem cells. *Nat Commun* **8**, 14744 (2017).
4. Mobasseri, S. A. *et al.* Patterning of human epidermal stem cells on undulating elastomer substrates reflects differences in cell stiffness. *Acta Biomaterialia* **87**, 256–264 (2019).
5. Hiratsuka, T., Bordeu, I., Pruessner, G. & Watt, F. M. Regulation of ERK basal and pulsatile activity control proliferation and exit from the stem cell compartment in mammalian epidermis. *Proc Natl Acad Sci USA* **117**, 17796–17807 (2020).
6. Yu, S.-M. Substrate curvature affects the shape, orientation, and polarization of renal epithelial cells. *Acta Biomaterialia* **77**, 311–321 (2018).

7. Yu, S.-M., Li, B., Granick, S. & Cho, Y.-K. Mechanical Adaptations of Epithelial Cells on Various Protruded Convex Geometries. *Cells* **9**, 1434 (2020).
8. Callens, S. J. P., Uyttendaele, R. J. C., Fratila-Apachitei, L. E. & Zadpoor, A. A. Substrate curvature as a cue to guide spatiotemporal cell and tissue organization. *Biomaterials* **232**, 119739 (2020).
9. Rougerie, P. *et al.* Topographical curvature is sufficient to control epithelium elongation. *Sci Rep* **10**, 14784 (2020).
10. Tomba, C. *et al.* Laser□Assisted Strain Engineering of Thin Elastomer Films to Form Variable Wavy Substrates for Cell Culture. *Small* **15**, 1900162 (2019).
11. Curtis, A. S. G. & Varde, M. Control of Cell Behavior: Topological Factors. *Journal of the National Cancer Institute* **33**, 15–26 (1964).
12. Dunn, G. A. & Heath, J. P. A new hypothesis of contact guidance in tissue cells. *Experimental Cell Research* **101**, 1–14 (1976).
13. Yevick, H. G., Duclos, G., Bonnet, I. & Silberzan, P. Architecture and migration of an epithelium on a cylindrical wire. *Proc Natl Acad Sci USA* **112**, 5944–5949 (2015).
14. Pieuchot, L. *et al.* Curvotaxis directs cell migration through cell-scale curvature landscapes. *Nat Commun* **9**, 3995 (2018).
15. Werner, M., Petersen, A., Kurniawan, N. A. & Bouten, C. V. C. Cell-Perceived Substrate Curvature Dynamically Coordinates the Direction, Speed, and Persistence of Stromal Cell Migration. *Adv. Biosys.* **3**, 1900080 (2019).
16. Barry, A. K. *et al.* -Catenin cytomechanics - role in cadherin-dependent adhesion and mechanotransduction. *Journal of Cell Science* **127**, 1779–1791 (2014).
17. Yu, F.-X. & Guan, K.-L. The Hippo pathway: regulators and regulations. *Genes & Development* **27**, 355–371 (2013).
18. Aragona, M. *et al.* A Mechanical Checkpoint Controls Multicellular Growth through YAP/TAZ Regulation by Actin-Processing Factors. *Cell* **154**, 1047–1059 (2013).
19. Hannezo, E., Prost, J. & Joanny, J.-F. Theory of epithelial sheet morphology in three dimensions. *Proceedings of the National Academy of Sciences* **111**, 27–32 (2014).
20. Okuda, S., Inoue, Y. & Adachi, T. Three-dimensional vertex model for simulating multicellular morphogenesis. *BIOPHYSICS* **12**, 13–20 (2015).
21. Hočevar Brezavšček, A., Rauzi, M., Leptin, M. & Ziherl, P. A Model of Epithelial Invagination Driven by Collective Mechanics of Identical Cells. *Biophysical Journal* **103**, 1069–1077 (2012).
22. Štorgel, N., Krajnc, M., Mrak, P., Štrus, J. & Ziherl, P. Quantitative Morphology of Epithelial Folds. *Biophysical Journal* **110**, 269–277 (2016).
23. Rupprecht, J.-F. *et al.* Geometric constraints alter cell arrangements within curved epithelial tissues. *MBoC* **28**, 3582–3594 (2017).
24. Fouchard, J. *et al.* Curling of epithelial monolayers reveals coupling between active bending and tissue tension. *Proceedings of the National Academy of Sciences* **117**, 9377–9383 (2020).
25. Wyatt, T. P. J. *et al.* Actomyosin controls planarity and folding of epithelia in response to compression. *Nat. Mater.* **19**, 109–117 (2020).
26. Broaders, K. E., Cerchiari, A. E. & Gartner, Z. J. Coupling between apical tension and basal adhesion allow epithelia to collectively sense and respond to substrate topography over long distances. *Integr. Biol.* **7**, 1611–1621 (2015).
27. Versaevel, M., Riaz, M., Grevesse, T. & Gabriele, S. Cell confinement: putting the squeeze on the nucleus. *Soft Matter* **9**, 6665–6676 (2013).
28. Elosegui-Artola, A. *et al.* Mechanical regulation of a molecular clutch defines force transmission and transduction in response to matrix rigidity. *Nat Cell Biol* **18**, 540–548 (2016).

29. Bruyère, C. *et al.* Actomyosin contractility scales with myoblast elongation and enhances differentiation through YAP nuclear export. *Sci Rep* **9**, 15565 (2019).
30. Mohammed, D. *et al.* Innovative tools for mechanobiology: unravelling outside-in and inside-out mechanotransduction. *Front. Bioeng. Biotechnol.* **7**, 162 (2019).
31. Hamouda, M. S., Labouesse, C. & Chalut, K. J. Nuclear mechanotransduction in stem cells. *Current Opinion in Cell Biology* **64**, 97–104 (2020).
32. Zhao, B. *et al.* Inactivation of YAP oncoprotein by the Hippo pathway is involved in cell contact inhibition and tissue growth control. *Genes & Development* **21**, 2747–2761 (2007).
33. Das, A., Fischer, R. S., Pan, D. & Waterman, C. M. YAP Nuclear Localization in the Absence of Cell-Cell Contact Is Mediated by a Filamentous Actin-dependent, Myosin II- and Phospho-YAP-independent Pathway during Extracellular Matrix Mechanosensing. *J. Biol. Chem.* **291**, 6096–6110 (2016).
34. Corne, T. D. J., Sieprath, T. & Vandenbussche, J. Deregulation of focal adhesion formation and cytoskeletal tension due to loss of A-type lamins. **11**, 447–463 (2017).
35. Wintner, O. *et al.* A Unified Linear Viscoelastic Model of the Cell Nucleus Defines the Mechanical Contributions of Lamins and Chromatin. *Adv. Sci.* **7**, 1901222 (2020).
36. Harada, T. *et al.* Nuclear lamin stiffness is a barrier to 3D migration, but softness can limit survival. *The Journal of Cell Biology* **204**, 669–682 (2014).
37. Shin, J.-W. *et al.* Lamins regulate cell trafficking and lineage maturation of adult human hematopoietic cells. *Proceedings of the National Academy of Sciences* **110**, 18892–18897 (2013).
38. Swift, J. *et al.* Nuclear Lamin-A Scales with Tissue Stiffness and Enhances Matrix-Directed Differentiation. *Science* **341**, 1240104–1240104 (2013).
39. Mascetti, G. *et al.* Effect of fixatives on calf thymocytes chromatin as analyzed by 3D high□resolution fluorescence microscopy. *Cytometry* **23**, 110–119 (1996).
40. Versaevel, M., Grevesse, T. & Gabriele, S. Spatial coordination between cell and nuclear shape within micropatterned endothelial cells. *Nat Commun* **3**, 671 (2012).
41. Vergani, L., Grattarola, M. & Nicolini, C. Modifications of chromatin structure and gene expression following induced alterations of cellular shape. *The International Journal of Biochemistry & Cell Biology* **36**, 1447–1461 (2004).
42. Harmand, N. & Hénon, S. 3D shape of epithelial cells on curved substrates. *arXiv:2005.07589 [cond-mat, physics:physics, q-bio]* (2020).
43. Miroshnikova, Y. A., Nava, M. M. & Wickström, S. A. Emerging roles of mechanical forces in chromatin regulation. *J Cell Sci* **130**, 2243–2250 (2017).
44. Nava, M. M. *et al.* Heterochromatin-Driven Nuclear Softening Protects the Genome against Mechanical Stress-Induced Damage. *Cell* **181**, 800-817.e22 (2020).
45. Pagliara, S. *et al.* Auxetic nuclei in embryonic stem cells exiting pluripotency. *Nature Mater* **13**, 638–644 (2014).
46. Kirkland, N. J. *et al.* Tissue Mechanics Regulate Mitotic Nuclear Dynamics during Epithelial Development. *Current Biology* **30**, 2419-2432.e4 (2020).
47. Buxboim, A. *et al.* Matrix Elasticity Regulates Lamin-A,C Phosphorylation and Turnover with Feedback to Actomyosin. *Current Biology* **24**, 1909–1917 (2014).
48. Koushki, N. *et al. Lamin A redistribution mediated by nuclear deformation determines dynamic localization of YAP*. http://biorxiv.org/lookup/doi/10.1101/2020.03.19.998708 (2020) doi:10.1101/2020.03.19.998708.
49. Owens, D. J. *et al.* Lamin Mutations Cause Increased YAP Nuclear Entry in Muscle Stem Cells. *Cells* **9**, 816 (2020).
50. Versaevel, M., Grevesse, T., Riaz, M., Lantoine, J. & Gabriele, S. Micropatterning Hydroxy-PAAm Hydrogels and Sylgard 184 Silicone Elastomers with Tunable Elastic

Moduli. *Micropatterning in Cell Biology Part C* **121**, 33–48 (2014).
51. Riaz, M., Versaevel, M., Mohammed, D., Glinel, K. & Gabriele, S. Persistence of fan-shaped keratocytes is a matrix-rigidity-dependent mechanism that requires α5β1 integrin engagement. *Sci Rep* **6**, 34141 (2016).
52. Grevesse, T., Versaevel, M., Circelli, G., Desprez, S. & Gabriele, S. A simple route to functionalize polyacrylamide hydrogels for the independent tuning of mechanotransduction cues. *Lab Chip* **13**, 777 (2013).
53. Sabnis, A., Rahimi, M., Chapman, C. & Nguyen, K. T. Cytocompatibility Studies of an in situ Photopolymerized Thermoresponsive Hydrogel Nanoparticle System using Human Aortic Smooth Muscle Cells. *Journal of Biomedical Materials Research Part A* **91**, 52–59 (2010).
54. Rabinovich, Y. *et al.* Atomic force microscopy measurement of the elastic properties of the kidney epithelial cells. *Journal of Colloid and Interface Science* **285**, 125–135 (2005).
55. Brückner, B. R. & Janshoff, A. Elastic properties of epithelial cells probed by atomic force microscopy. *Biochimica et Biophysica Acta* **1853**, 3075–3082 (2015).
56. Kocgozlu, L. *et al.* Selective and uncoupled role of substrate elasticity in the regulation of replication and transcription in epithelial cells. *Journal of Cell Science* **123**, 29–39 (2010).
57. Pietuch, A. *et al.* Mechanical properties of MDCK II cells exposed to gold nanorods. **6**, 223–231 (2015).
58. Alaimo, L. *et al.* Engineering slit‐like channels for studying the growth of epithelial tissues in 3D‐confined spaces. *Biotechnology and Bioengineering* **117**, 2887–2896 (2020).
59. Mohammed, D. *et al.* Substrate area confinement is a key determinant of cell velocity in collective migration. *Nat. Phys.* **15**, 858–866 (2019).
60. Schneider, C. A., Rasband, W. S. & Eliceiri, K. W. NIH Image to ImageJ: 25 years of image analysis. *Nat Methods* **9**, 671–675 (2012).

Figure 1 – Wavy epithelial monolayers on corrugated polyacrylamide hydrogels. (A) Schematic representation of an epithelial monolayer grown on a corrugated hydrogel of amplitude, β, and wavelength, λ. The corrugated profile is composed of crests (convex curvature), intermediate, or interm., zones (zero curvature) and valleys (concave curvature). The balance between apical tension (Γ_a, in green), lateral tension (Γ_l, in red) and basal tension (Γ_b, in brown) leads to the thickness modulation of the epithelial monolayer, changes of nuclear morphologies and nuclear offsets. (B) Confocal volume rendering of a MDCK epithelial monolayer stained for F-actin (in green) and nuclei (in blue) grown on corrugated substrates of 20 μm (λ20 in grey), 30 μm (λ30 in red) and 50 μm (λ50 in blue) wavelength. Scale bars are 20 μm. (C) Confocal volume rendering of the nuclei in epithelial monolayers grown on corrugated substrates of 20 μm (λ20 in grey), 30 μm (λ30 in red) and 50 μm (λ50 in blue) wavelength. The height is color-coded. Scale bars are 20 μm.

Figure 2 – Theoretical modelling of epithelial thickness modulations from substrate curvature. (A) Equilibrium configuration of a 2D vertex model representing apical and lateral surfaces of an epithelial monolayer attached to a curved substrate. Increasing substrate wavelength, λ, decreased epithelial thickness modulations. (B) From top to bottom: representative confocal profiles (*xz*) and average thickness modulation for λ20 (in grey), λ30 (in red) and λ50 (in blue) corrugated hydrogels (N=8 replicates for each condition) calculated by subtracting apical and basal position of wavy epithelial monolayers at given position *x*. (C) Thickness modulation versus a rescaled wavevector (Δh/λ) for experimental data (mean± S.D.) λ20 (in grey, N=6 replicates), λ30 (in red, N=5 replicates) and λ50 (in blue, N=6 replicates) with the fit from the model (dashed lines correspond to S.D.).

Figure 3 – Substrate curvature modulates the spatial distribution of nuclei. (A) Typical confocal image of an epithelial monolayer grown on a λ50 corrugated hydrogels stained for cadherins (in red) and DNA (nuclei, in grey). The zoom panel shows the position of the nuclear center (X in grey) relative to the cellular center (X in blue) as a function of thickness gradients, tending to attract nuclei from intermediate zones to concave ones (valleys). The vector (in red) between the center of mass of cells and nuclei represents the nuclear offset. (B) Sketch of the nuclear offset (arrow in red) determined from the difference between cellular and nuclear axis (lateral view). (C) Experimental and theoretical nuclear offsets versus the coordinate along the *x* axis normalized by the wavelength for λ20 (grey squares), λ30 (red circles) and λ50 (blue triangles) corrugated substrates. $109 \leq n \leq 162$ per sample with N=3 replicates per condition. The dashed line on λ20 corresponds to the best fit. (D-G) 2D vertex models (see Supplementary Theory Note) incorporating nuclear positioning (force proportional to thickness gradients, taking cells away from equilibrium center position) for (D) λ=1.5 and (F) λ=2. Nuclei are predicted to be positioned towards concave zones, an effect particularly accentuated for wavelengths at integer values of cell width (λ=2). Typical DIC images of (E) λ20 and (G) λ30 wavy hydrogels with the automatic detection (in yellow) of the nuclei stained with DAPI.

Figure 4 – YAP-curvature sensing is mediated by nuclear density modulation. (A) From left to right: fluorescent images of confluent epithelial monolayers (1.10^3 cells/mm^2) on flat, λ20, λ30 and λ50 hydrogels and at high cell density (5.10^4 cells/mm^2) on λ20 and flat hydrogels. Tissues were stained for YAP (in red) and DNA with DAPI (in blue) after 48 hours in culture. Scale bars are 30 µm. Nuclear to cytoplasmic YAP ratio on convex (crest) and concave (valley) zones of λ20 (grey), λ30 (red) and λ50 (blue) corrugated hydrogels for (B) normal (1.10^3 cells/mm^2) and (C) high (5.10^4 cells/mm^2) cellular densities. Black bars correspond to flat hydrogels (n=46, N=3 replicates). For normal cell density n=24 (λ20), n=12 (λ30) and n=12 (λ50) with $3 \leq N \leq 8$ replicates. For high cell density n=16 (λ20), n=22 (λ30) and n=10 (λ50) with $3 \leq N \leq 8$ replicates. (D) Nuclear to cytoplasmic YAP ratio versus local nuclear density on flat (circles), convex (triangles) and concave (squares) zones. All data are shown as mean ± S.D. *$p < 0.05$, and n.s. not significant.

Figure 5 – Composition of the nuclear lamina depends on substrate curvature. (A) Maximum intensity projection of the nuclei of a MDCK epithelial monolayer grown on a λ20 corrugated hydrogel and stained with DAPI (in blue), lamin A/C (LMAC, in red) and lamin B1 (LMB1, in green). Merge image of LMAC and LMB1. The scale bar is 20 µm. White rectangles correspond to nuclei located on convex, interm. and concave zones. (B) Typical confocal volume views (*xz* view) of a nucleus on convex (crest), interm. and concave (valley) zones. Z_0 (basal), Z_1 (mid-height) and Z_2 (apical) zones are indicated in orange. (C) Typical maximum intensity projection (*xy* view) of a nucleus on convex (crest), an interm. and a concave (valley) zones and stained with DAPI in blue, LMAC in red and LMB1 in green. (D) LMA/LMB intensity ratio versus nuclear height of nuclei on convex (crest), interm. and concave (valley) zones. Black arrows indicate Z_0 (basal), Z_1 (mid-height) and Z_2 (apical) zones. (E) Schematic representation of the balance between LMAC (in red) and LMB1 (in green) for nuclei on convex, interm. and concave (valley) zones. All data are shown as mean ± S.D. with n=4 nuclei per replicate (N=3).

Figure 6 – Concave curvature zones lead to lower cell proliferation rate and promote significant chromatin condensation in elongated nuclei. (A) Schematic of the model used to predict nuclear deformations and volume changes, for an axisymmetric compressed nucleus (in blue) with r and z the nuclear coordinates, θ the angle between the local tangent of the nuclear profile and r-axis, d_b the radius of the contact zone between nucleus and plane and s the arclength of the nuclear profile (see Supplementary Note for details). The insert shows a side (yz) confocal volume view of a nucleus on top of a crest zone, i.e. vertically compressed. (B) Normalized nuclear volume versus normalized cell height shows that nuclear deformations are generically associated to volume reductions. Black squares are Finite Element Model (FEM) simulation, black line the exact solution and red dashed line the analytical approximation. Nuclear volume on interm., concave and convex zones of (C) λ20 (in grey, n=24 with N=3 replicates) and (D) λ30 (in red, n=33 with N=3 replicates) corrugated hydrogels. (E-F) Typical successive changes (from bottom to top) of the level of chromatin condensation on concave curvature zones of (E) λ20 and (F) λ30 corrugated hydrogels. Intensities of DNA staining were digitized in 256 bits and color coded for each Z-stack. Highly condensed domains show higher fluorescence intensity with respect to the less condensed ones. (G-H) Chromatin to nuclear volume ratio for cells on interm., concave and convex zones on (G) λ20 (in grey, n=20 with N=3 replicates) and (H) λ30 (in red, n=29 with N=3 replicates) corrugated hydrogels. (I) Typical images of DAPI (in blue) and Edu (in red) staining in an epithelial monolayer grown on λ20 (top row) and λ30 (bottom row) corrugated hydrogels. Scale bars are 20 μm. Rate of Edu-positive cells on (J) convex (n=22 with N=3 replicates) and (K) concave (n=22 with N=3 replicates) curvature zones. Dark gray bars are flat hydrogels, light gray bars λ20 and red bars λ30. All data are shown as mean ± S.D. *p < 0.05, **p < 0.01, ***p < 0.001, ****p < 0.0001 and n.s. not significant.

Extended Data Figure 1 – Curvature of corrugated hydroxy-PAAm hydrogels. (A) Representation of a 3D volume view of a corrugated substrate with a tangent plane (*xy*, in blue) and two planes of principal curvatures: *xz* in green (k_1=1/R) and *yz* in red (k_2=0). The Gaussian curvature is $k_1.k_2$=0. The inset shows a 3D confocal view of a λ30 corrugated epithelial monolayer immunostained for actin (in green) and DNA (in blue). The scale bar is 30 µm. (B) Top: confocal view (xz) of the wavy profile of a corrugated epithelial monolayer (λ30) immunostained for actin (in green) and DNA (in blue). The scale bar is 10 µm. Bottom: Schematic representation of the wavy profile of a corrugated epithelial monolayer composed of concave (in blue), interm. (in green) and convex (in orange) zones. Convex zones correspond to the crest and concave zones to the valley. Interm. zones of zero curvature were located between concave and convex zones and the tangent to the interm. zones was used to determine borders with concave and convex zones. (C) The curvature, C, of convex (crest, in orange) and concave (valley, in blue) zones was determined along the substrate profile (xz, in black) as the reciprocal of the radius (C=1/R) of the osculating circle having its center lying on the normal line. The substrate profile is characterized by a wavelength λ and an amplitude β.

Name	Wavelength ± SD (μm)	Convex curvature (μm^{-1})	Concave curvature (μm^{-1})	Amplitude ± SD (μm)
λ20/1.2	20.6 ± 0.9	0.13	- 0.58	1.2 ± 0.1
λ20/2.3	20.1 ± 0.6	0.09	- 0.29	2.3 ± 0.6
λ30/2.3	30.1 ± 0.1	0.27	- 0.27	2.3 ± 0.1
λ50/2.4	49.9 ± 1.0	0.02	- 0.11	2.4 ± 0.8
λ50/3.2	50.2 ± 0.7	0.03	- 0.08	3.2 ± 0.5

Extended Data Table 1 – Dimensions of the corrugated hydrogels. Wavelength (λ), convex curvature (crest), concave curvature (valley), and amplitude (β) of λ20 (n=12), λ30 (n=11), λ50 (n=12), λ20/4.5 (n=11), λ50/4.6 (n=11) corrugated hydrogels were determined on swollen hydroxy-PAAm hydrogels by atomic force microscopy (AFM) in liquid mode at 37°C. Mean ± S.D.

Extended Data Figure 2 – Corrugations do not affect the actin intensity of epithelial monolayer. (A) Maximum intensity projection of an epithelial monolayer grown on a flat, λ20 (in grey), λ30 (in red) and λ50 (in blue) hydrogel and stained for F-actin (in green) and nuclei (in blue). Scale bars are 20 μm for flat and λ20, 30 μm for λ30 and 50 μm for λ50. (B) High magnification confocal images of valley and crest zones for λ20, λ30 and λ50 corrugated hydrogels stained for actin (in green) with AlexaFluor 488. (C) 3D volume rendering of a MDCK monolayer grown on a flat hydroxy-PAAm hydrogel coated with FN. Actin is labeled in green with AlexaFluor 488 and DNA in blue with DAPI. The scale bar is 50 μm. (D) Total actin intensity in epithelial tissues grown on flat (dark grey), λ20 (light grey), λ30 (red) and λ50 (blue) hydrogels. n=8 (flat in black), n=10 (λ20 in grey), n=12 (λ30 in red) and n = 5 (λ50 in blue). n.s. is not significant.

Extended Data Figure 3 – Mean epithelial cell area and polygon class. Typical maximum intensity projection image of a MDCK monolayer stained for ß-catenin and grown on (A) λ20, (B) λ30 and (C) λ50 corrugated hydrogels and corresponding skeleton image of (D) λ20, (E) λ30 and (F) λ50. Scale bars correspond to 100 µm (λ20 and λ30) and to 50 µm (λ50). (G) Mean cell area and (H) distribution of polygon classes of epithelial tissues grown on flat (black), λ20 (grey), λ30 (red) and λ50 (blue) hydrogels. n= 1100 cells (flat in black), 1500 cells (λ20 in grey), 1700 cells (λ30 in red) and 1050 cells (λ50 in blue), obtained from n=3, n=6, n=5 and n=3 replicates respectively. (I) Mean cell area versus polygon class of epithelial monolayers grown on flat (black), λ20 (grey) and λ30 (red) hydrogels. n.s. is not significant.

Extended Data Figure 4 – Schematic of the model and sensitivity analysis. Equilibrium configuration of a 2D vertex model representing apical and lateral surfaces of an epithelial monolayer attached to a curved substrate. (A) Decreasing substrate amplitude, β, or (B) decreasing apical tensions, Γ_a, decreased thickness modulations. (C) Simulation of the vertex model on curved substrate with increasing density (4, 6, and 8 cells per wavelength, from top to bottom), showing that increasing density decreases thickness modulations. (D) Simulation of human keratocyte on curved substrate (see Supplementary Note for details), modelled with $\frac{\Gamma_a}{\Gamma_l} \approx 5$, showing density modulations even for large wavelengths (top), which are amplified further to the point of crest/top dewetting when doubling the substrate amplitude (middle), or when doubling apical tensions $\frac{\Gamma_a}{\Gamma_l} \approx 10$ (bottom). (E) Comparison for the thickness modulation Ω between analytical theory (thin lines) and vertex simulations (dots), for $\frac{\Gamma_a}{\Gamma_l} = 5$ (purple), $\frac{\Gamma_a}{\Gamma_l} = 2$ (green) and $\frac{\Gamma_a}{\Gamma_l} = 1$ (purple), showing good agreement for large wavelengths λ (normalized by average cell thickness Δh, in all panels C-E, we have taken for simplicity average cell thickness $\Delta h = 1$ and average cell side length $2d = 1$), with corrections for small wavelengths. (F) Schematics of contact mechanics model of a nucleus subjected to apical compression, before (left) or after (right) lateral contact. (G-I) Sensitivity analysis of different model parameters/observations. Both full solutions (solid line) and analytic approximations (dashed line) are given (see Supplementary Note for details). We examine the influence of normalized cell height □ on aspect ratio S_n (G) for the nucleus (volume ratio of cell to nucleus $\bar{v} = \frac{V_c}{\pi r_0^2} = 2$ and before lateral contact). We also examine the influence of local thickness gradient on aspect ratio (H) and nuclear offset (I), with □ = 0.5, $\bar{d} = 1.57$, and tension ratio $\frac{\Gamma_a}{\Gamma_{n0}} = 5$. We find on both metrics a sharp transition above a critical value of thickness gradients, which occurs when the nucleus reaches lateral contact (and thus cannot

increase its offset but start adopting distorted asymmetric shape because of the asymmetric contact).

Extended Data Figure 5 – Modulation of wavelength and amplitude of corrugated substrates. (A) Representative 3D confocal image of the spatial localization of the nuclei within an epithelial monolayer grown on a corrugated hydroxy-PAAm hydrogels of 100 µm in wavelength (λ100). The nuclear height is color-coded. (B) From top to bottom**:** typical confocal profile of an epithelial monolayer grown for 48 hours on a corrugated λ100 substrates and stained for actin with phalloidin. Average height profiles along the x position obtained from Z-stack confocal imaging (n=5). Vertex model showing the thickness modulation of the epithelial monolayer with thicker cells on convex zones and thinner ones on concave zones. (C) Modulation of the corrugation amplitude for λ20 (in grey) and λ50 (in blue) substrates to match the amplitude of λ30 (in red) substrates of ~2.3 µm. The amplitude of λ20 substrates was increased to ~2.3 µm (λ20/2.3, n=16 with N=3 replicates) and the amplitude of λ50 substrates was decreased to ~2.4 µm (λ20/2.4, n=18 with N=3 replicates) (B) Thickness modulation of the epithelial monolayer for λ20 (in grey) and λ50 (in blue) substrates of different amplitudes. **p < 0.01, ***p < 0.001, ****p < 0.0001 and n.s. not significant.

Extended Data Figure 6 – Substrate curvature modulates the nuclear area. (A) Local nuclear projected area normalized by the mean nuclear area of each sample on convex (crest) and concave (valley) zones of λ20 (grey), λ30 (red) and λ50 (blue) substrates. (B) Nuclear density normalized by the mean nuclear density of each sample on convex and concave zones of λ20 (grey), λ30 (red) and λ50 (blue) substrates. 109≤n≤162 nuclei per sample with N=3 replicates for all conditions. **p < 0.01 and ***p < 0.001. (C-E) Local nuclear projected area (normalized by overall mean nuclear area) versus normalized position (*x* axis normalized by the wavelength, so that 0 and 1 correspond to top/concave regions and 0.5 to bottom/convex regions) for epithelial monolayers grown on (C) λ20, (D) λ30 and (E) λ50 hydrogels, for the best fit parameter of $\gamma = 0.25\ \mu m^{-1}$ (see Supplementaty Note for details). Grey squares (λ20), red circles (λ30) and blue triangles (λ50) are experimental data (mean ± S.D.) and plain lines the best fit model. 109≤n≤162 nuclei per sample with 3 replicates for all conditions.

Extended Data Figure 7 – Nuclear orientation and YAP nuclear export are modulated by substrate concave curvatures. Mean orientation of the nuclei on (A) convex (crest) and (B) concave (valley) curvature zones of λ20 (in grey), λ30 (in red) and λ50 (in blue) wavy hydrogels. All data are shown as mean ± SD. The number of nuclei is indicated at the bottom of each bar: 170≤n≤368 for concave curvature and 109≤n≤405 for convex curvature. Nuclear to cytoplasmic YAP ratio of nuclei on interm., concave, convex zones of (C) λ20 in grey, (B) λ30 in red and (C) λ50 in blue corrugated hydrogels. Black bars correspond to flat hydrogels. For λ20 n=30 (interm.), n=16 (concave), 24 (convex) and n=50 (flat) obtained from 5 to 7 replicates, for λ30 n=18 (interm.), n=18 (concave), n=9 (convex) and n=50 (flat) obtained from 5 to 9 replicates and for λ50 n=6 (concave), n=7 (convex) and n=50 (flat) obtained from 3 to 5 replicates. All data are shown as mean ± SD. *p < 0.1, **p < 0.01, ***p < 0.001, ****p < 0.0001 and n.s. not significant.

Extended data Figure 8. Finite element simulations of nuclei on curved substrates. (A) Snapshots of nuclear 3D morphologies in different regions, with the normalized average monolayer thickness $\Delta\bar{h}$=0.3. Dependence of (B) the normalized nuclear volume $\bar{V}_n$ and (C) the nuclear aspect ratio in x-y plane on $\Delta\bar{h}$. A nucleus in the concave region is either in contact with the neighboring nucleus (or cell membrane) on the right side, or confined on both sides, with cell side length (along x-axis) proportional to monolayer thickness.

Extended data Figure 9. Large-scale curvature sensing by epithelial monolayers depends on active cell mechanics and nuclear mechanoadaptation. Schematic representation of the epithelial thickness modulation and the three main nuclear morphologies observed on crest (convex), interm. zones and valleys (concave). Composition of the nuclear lamina depends on substrate curvature, whereas YAP-curvature sensing is mediated by nuclear density modulation. Concave curvature zones lead to lower cell proliferation rate and promote significant chromatin condensation in elongated nuclei.

A

λ

β

CREST
(convex)

INTERM
(zero curvature)

VALLEY
(concave)

Epithelial
thickness

Convex

Concave

↔ Apical surface Ta

↔ Lateral surface Tℓ

↔ Basal surface Tb

Nuclear morphology
and offset

B

λ20

λ30

λ50

C

λ20

8 µm
6 µm
4 µm
2 µm
0 µm

λ30

12 µm
10 µm
8 µm
6 µm
4 µm
2 µm
0 µm

λ50

12 µm
10 µm
8 µm
6 µm
4 µm
2 µm
0 µm

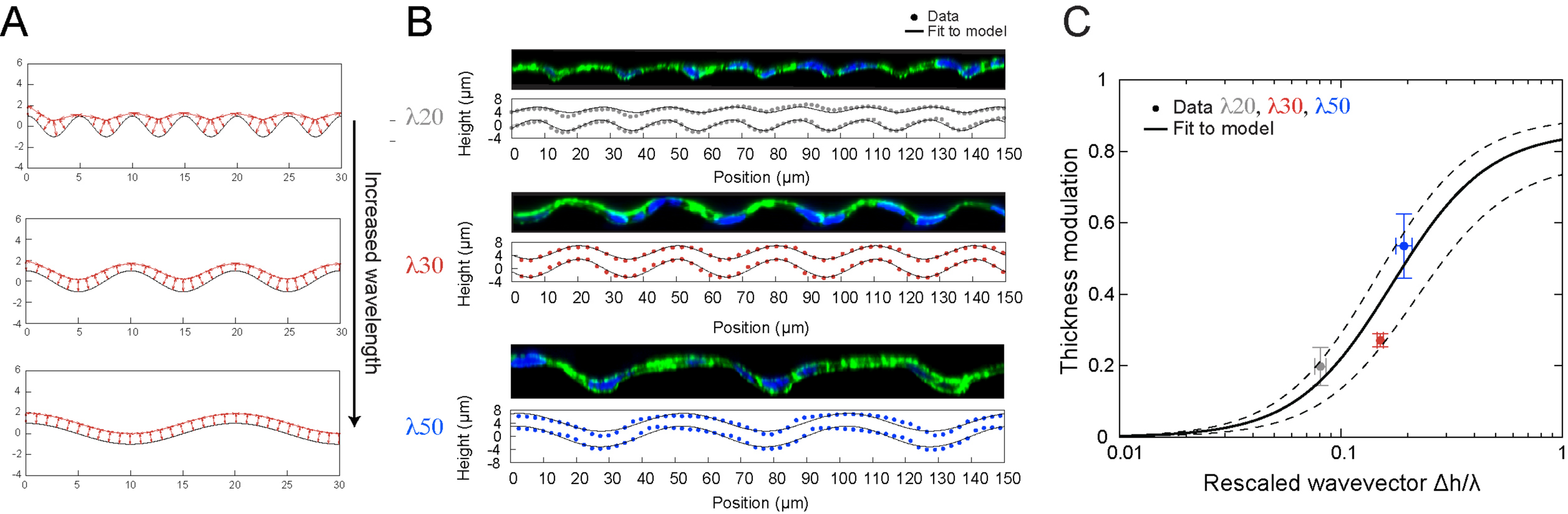
A
Increased wavelength
B
Data
Fit to model
λ20
λ30
λ50
Height (μm)
Position (μm)
C
Data λ20, λ30, λ50
Fit to model
Thickness modulation
Rescaled wavevector Δh/λ

A

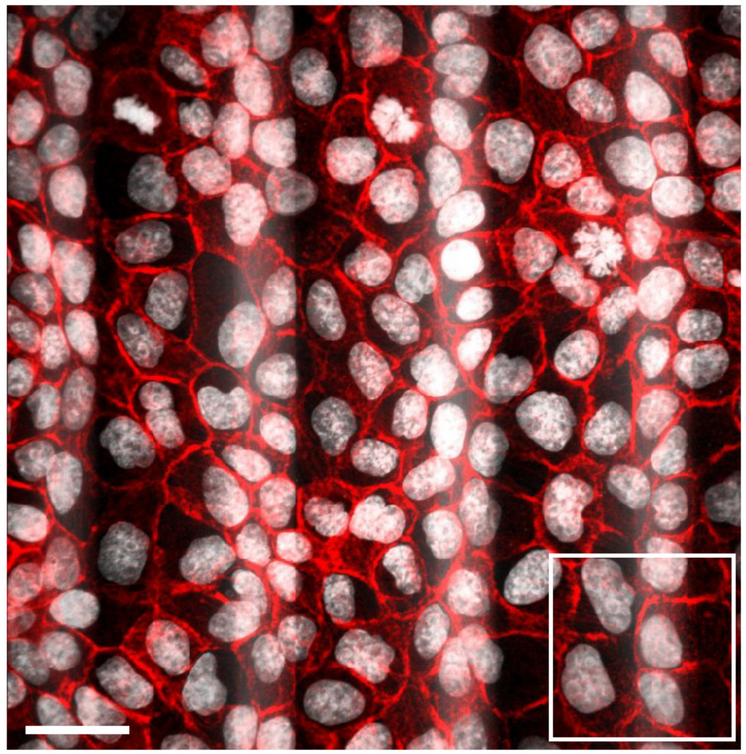

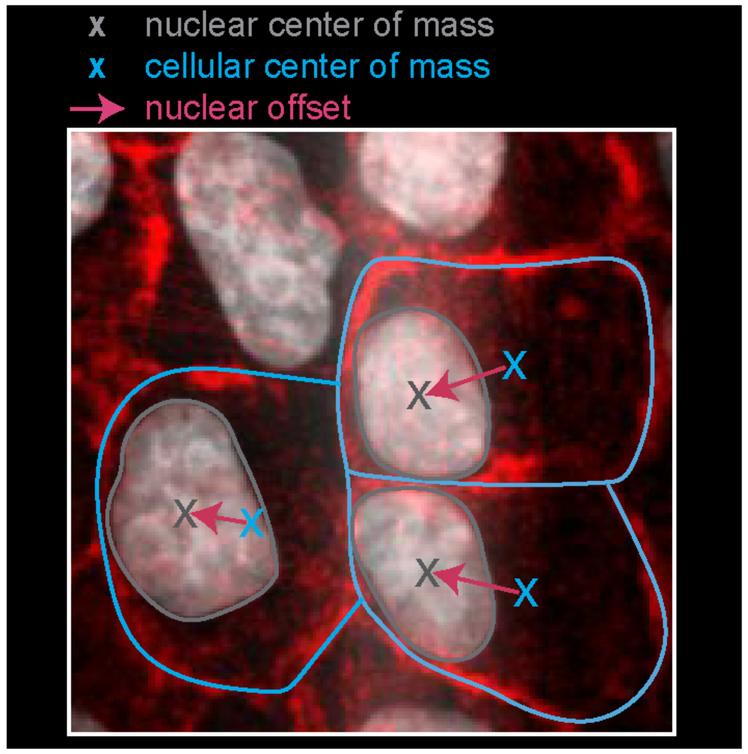
nuclear center of mass
cellular center of mass
nuclear offset

B

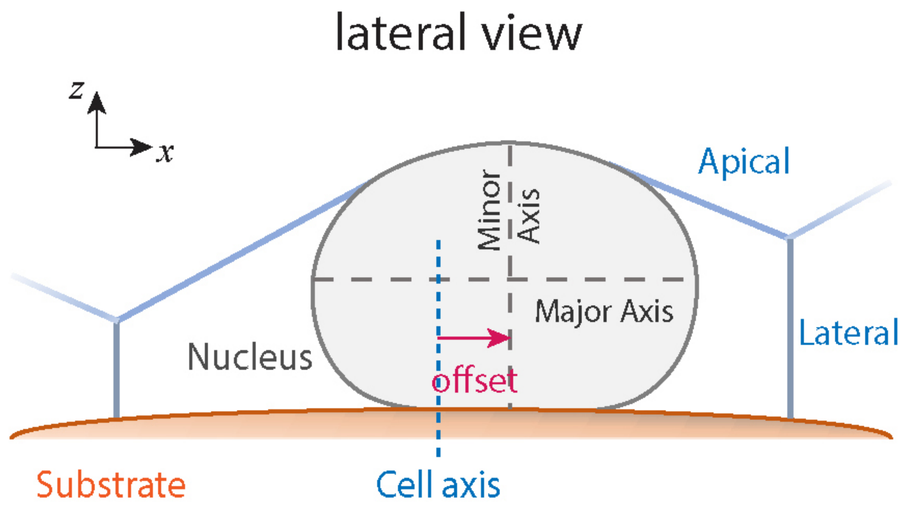
lateral view
z
x
Apical
Minor Axis
Major Axis
Nucleus
offset
Lateral
Substrate
Cell axis

C

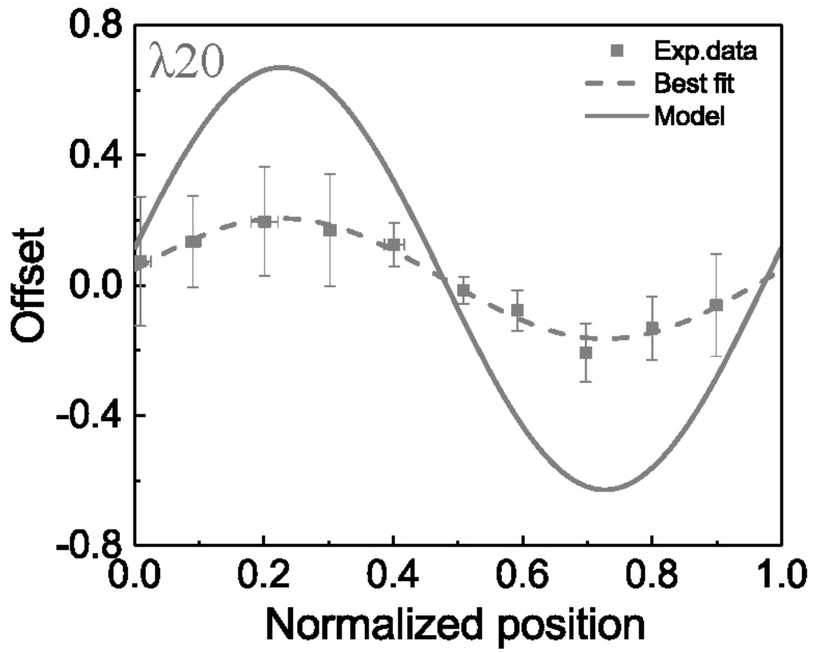
λ20
Exp.data
Best fit
Model
Offset
Normalized position

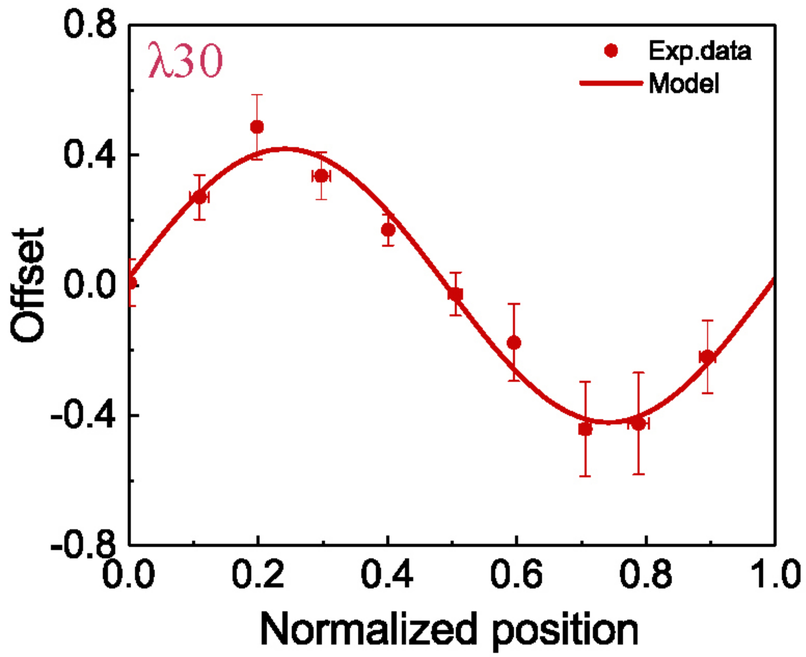
λ30
Exp.data
Model
Offset
Normalized position

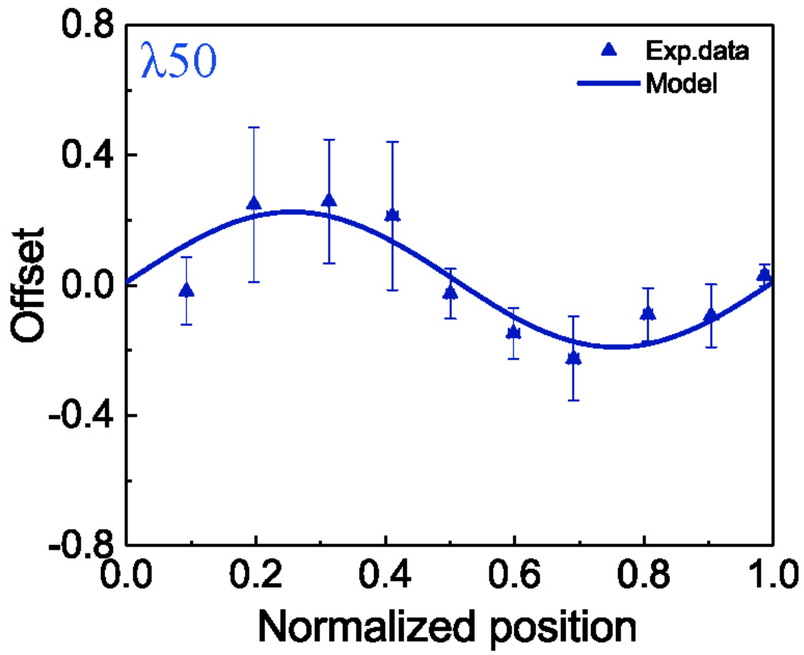
λ50
Exp.data
Model
Offset
Normalized position

D

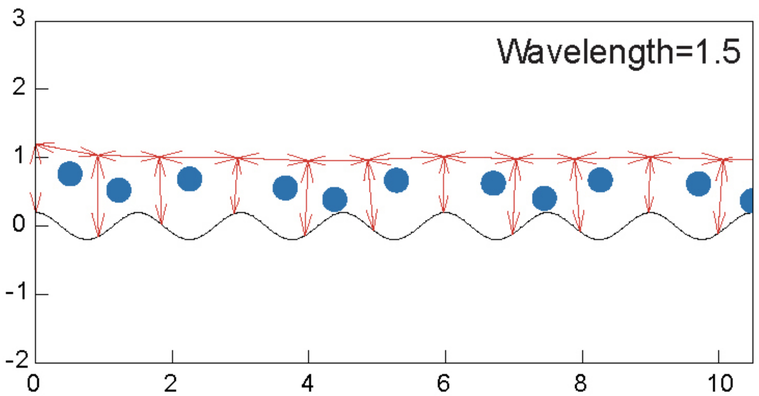
Wavelength=1.5

E

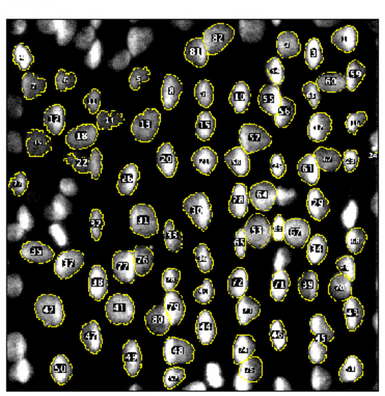

F

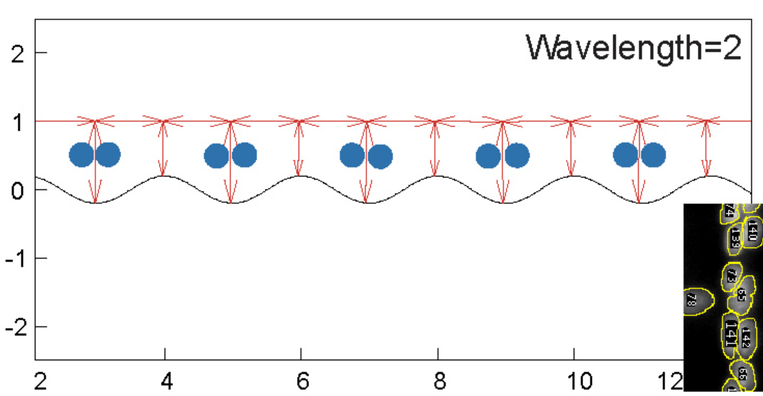
Wavelength=2

G

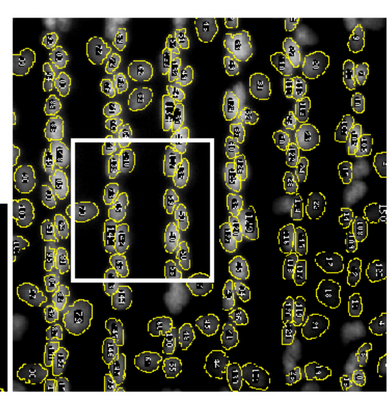

A

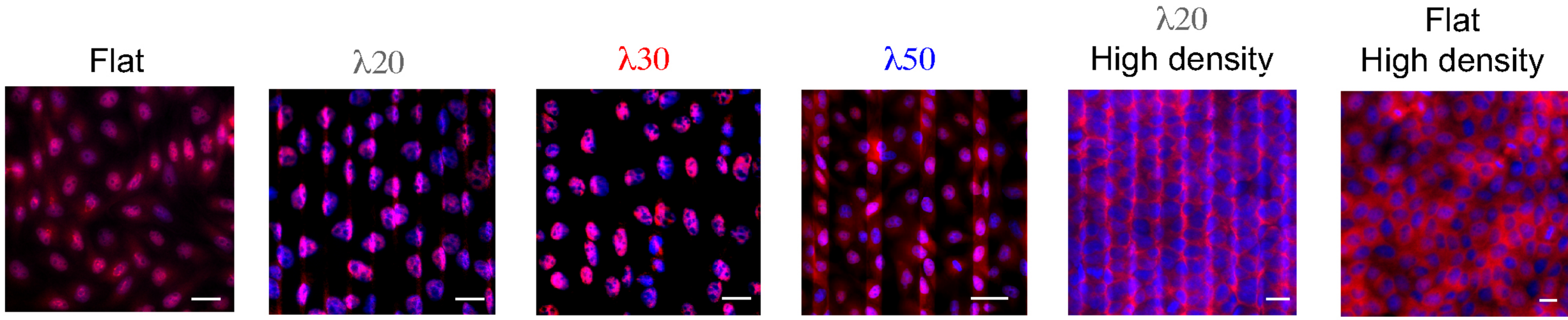
Flat
λ20
λ30
λ50
λ20
High density
Flat
High density
DAPI + YAP

B

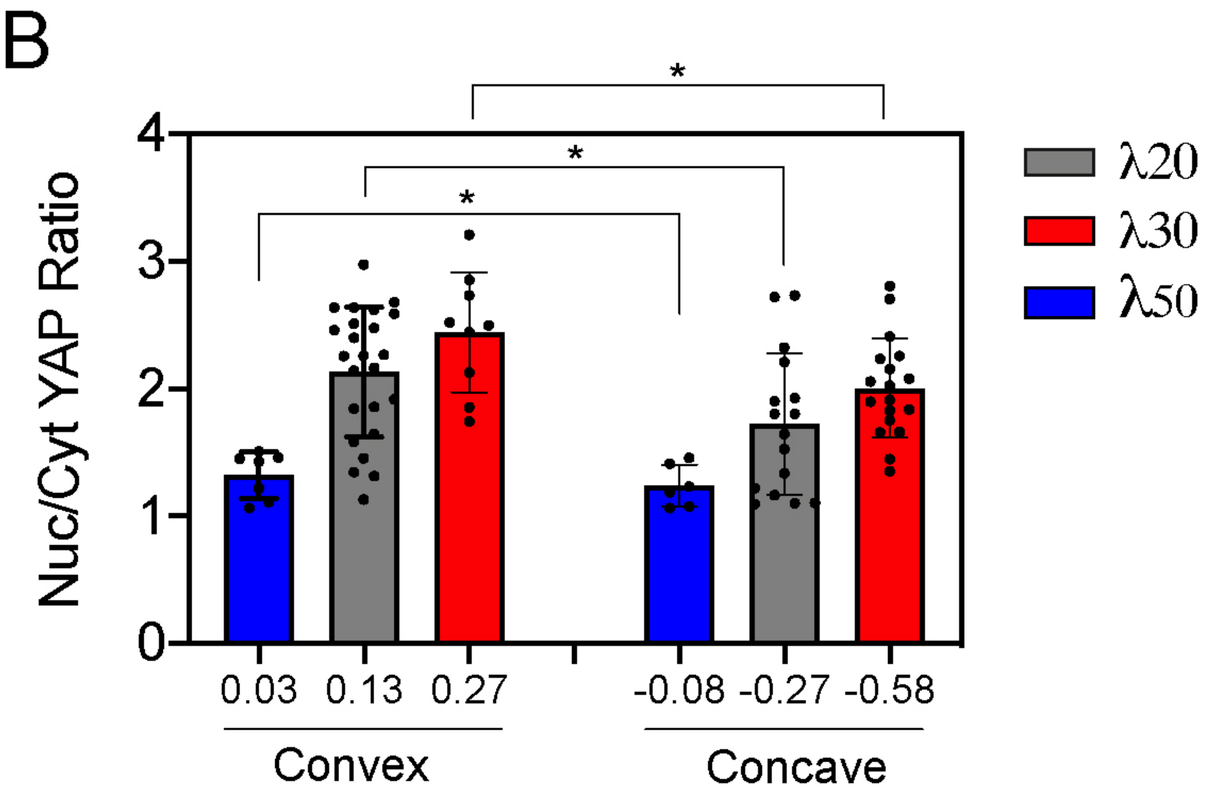
Nuc/Cyt YAP Ratio
0
1
2
3
4
*
*
*
λ20
λ30
λ50
0.03 0.13 0.27
-0.08 -0.27 -0.58
Convex
Concave

C

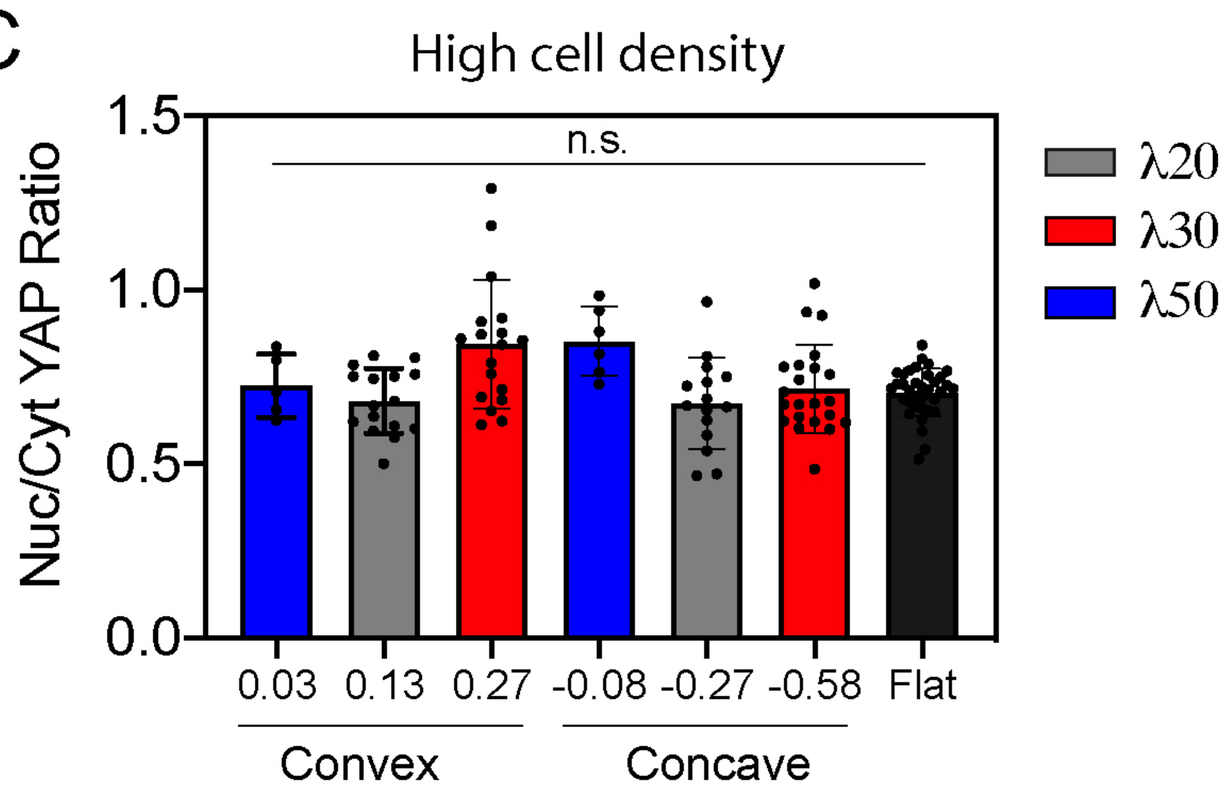
High cell density
Nuc/Cyt YAP Ratio
0.0
0.5
1.0
1.5
n.s.
λ20
λ30
λ50
0.03 0.13 0.27
-0.08 -0.27 -0.58
Flat
Convex
Concave

D

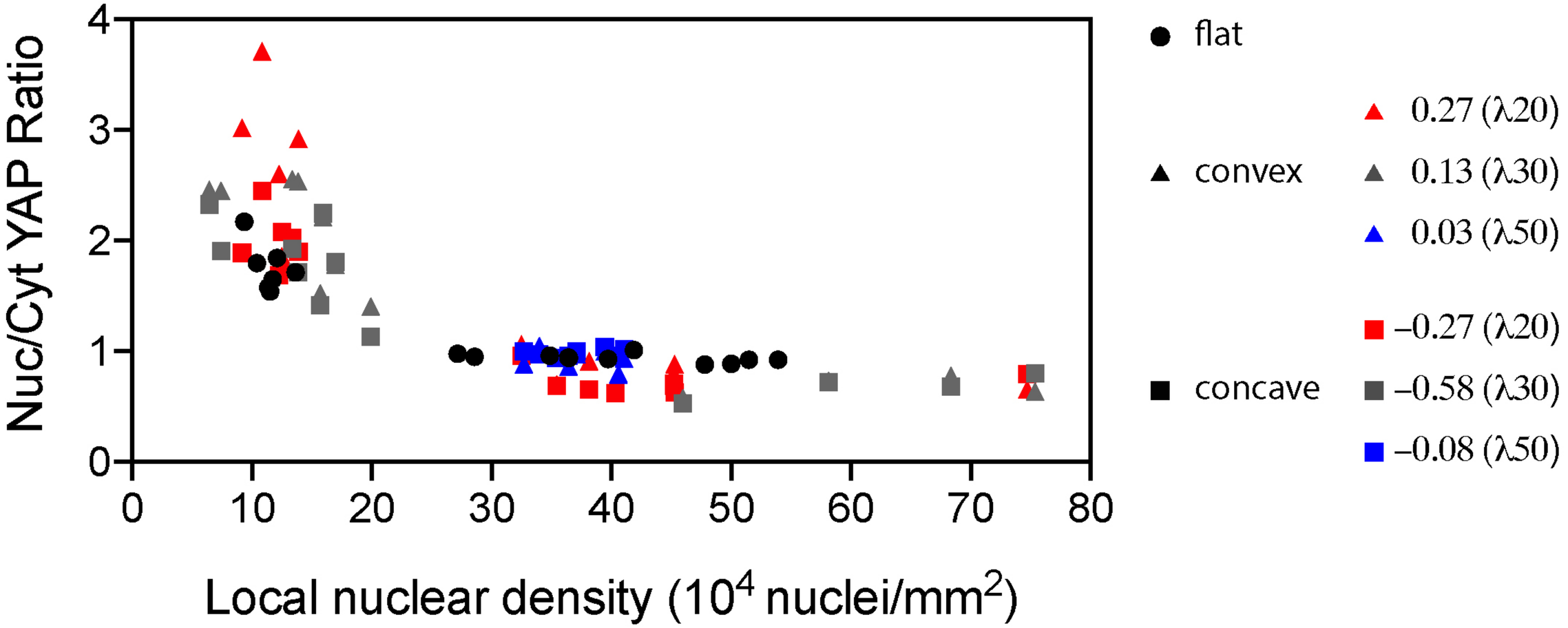
Nuc/Cyt YAP Ratio
0
1
2
3
4
0
10
20
30
40
50
60
70
80
Local nuclear density (10^4 nuclei/mm^2)
flat
convex
concave
0.27 (λ20)
0.13 (λ30)
0.03 (λ50)
–0.27 (λ20)
–0.58 (λ30)
–0.08 (λ50)

A

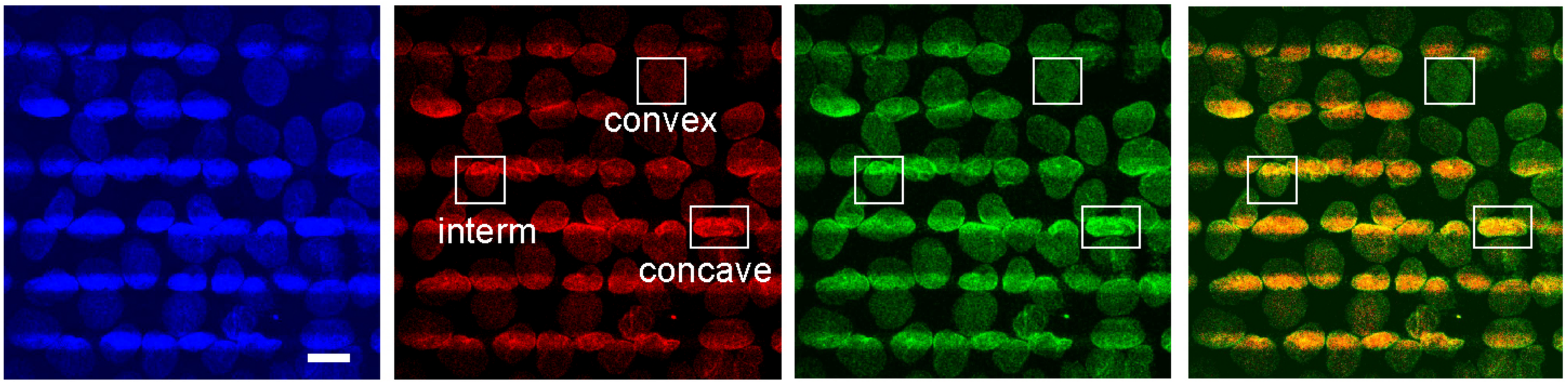
DAPI
LMAC
LMB1
LMAC + LMB1
convex
interm
concave

B

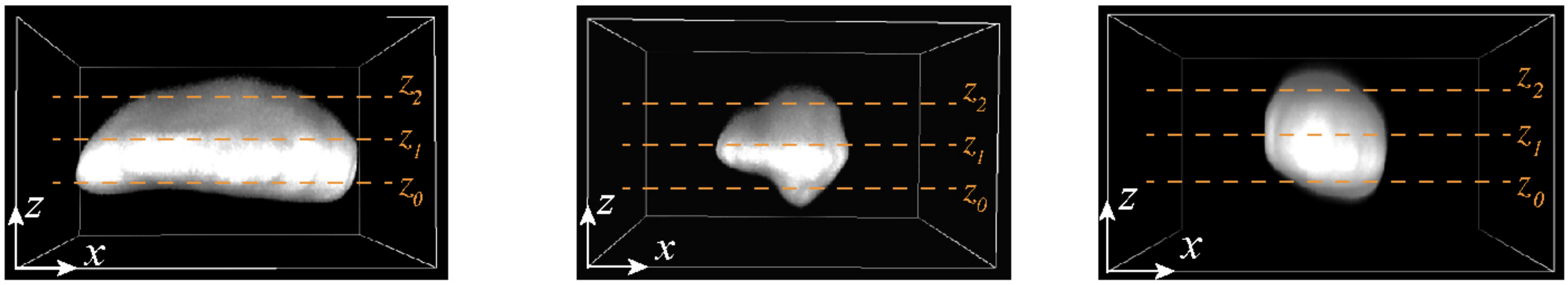
convex
interm
concave
z_2
z_1
z_0
z
x

C

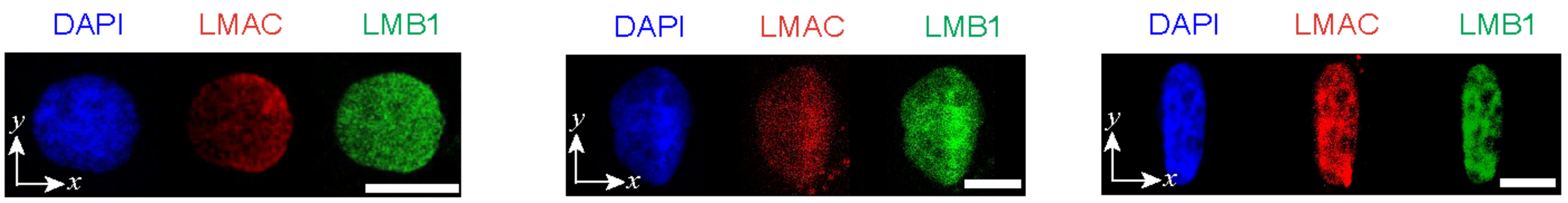
DAPI
LMAC
LMB1
y
x

D

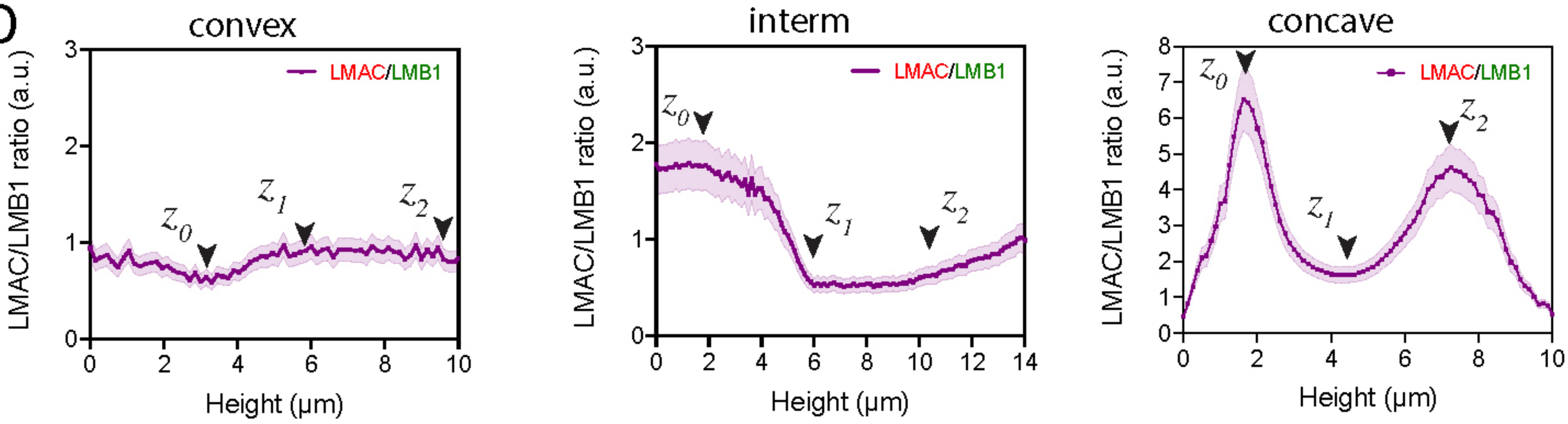
convex
interm
concave
LMAC/LMB1
LMAC/LMB1 ratio (a.u.)
Height (μm)
z_0
z_1
z_2

E

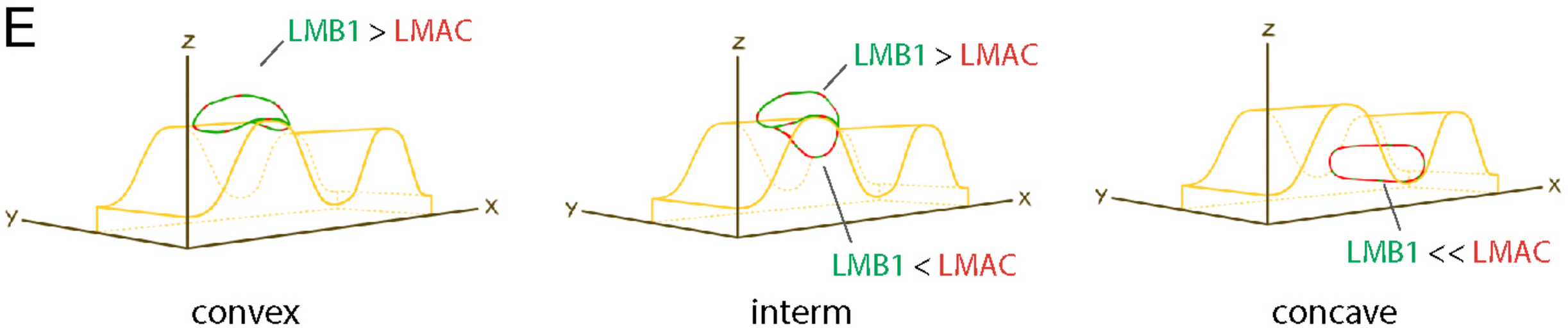
LMB1 > LMAC
LMB1 < LMAC
LMB1 << LMAC
z
y
x
convex
interm
concave

A

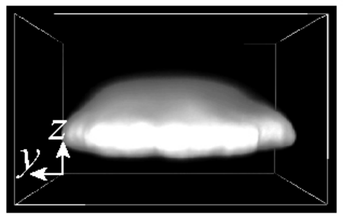

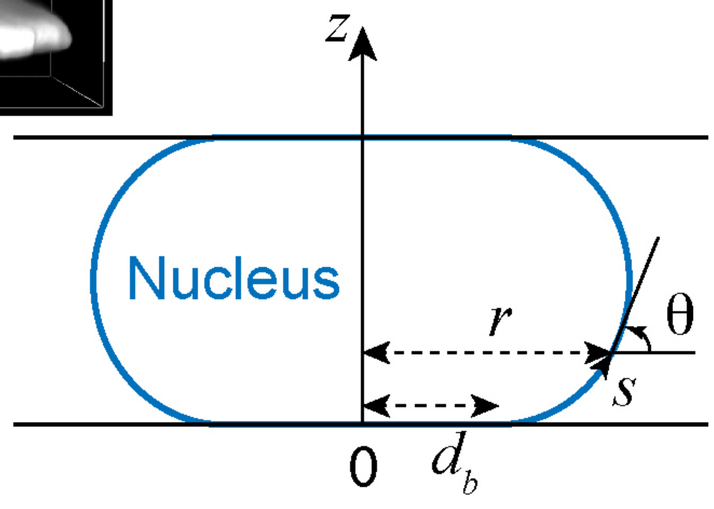

B

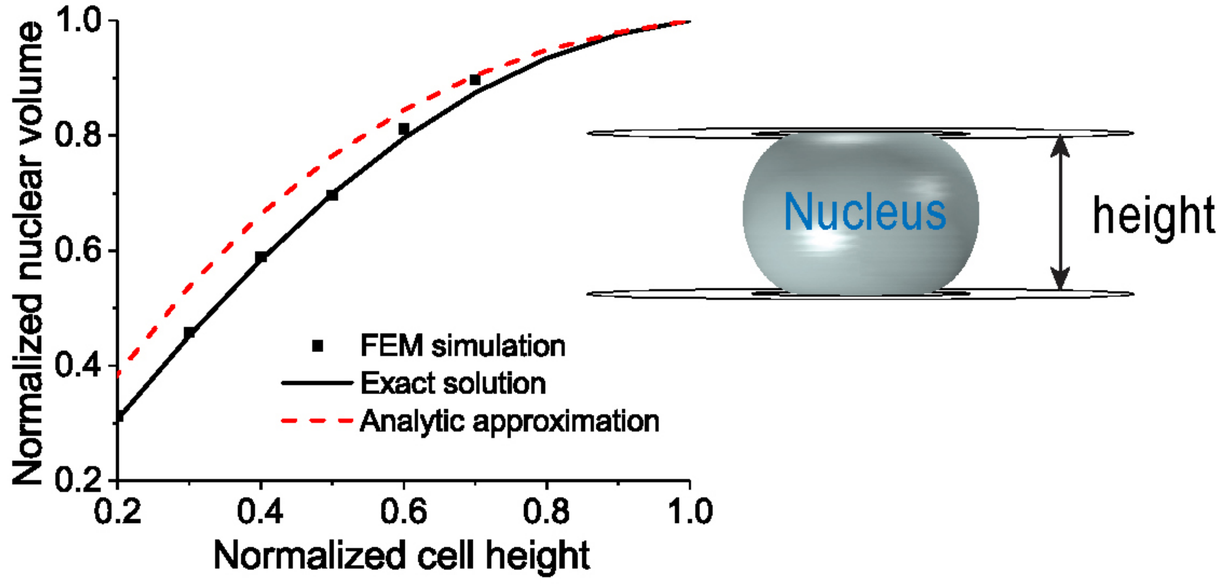

C

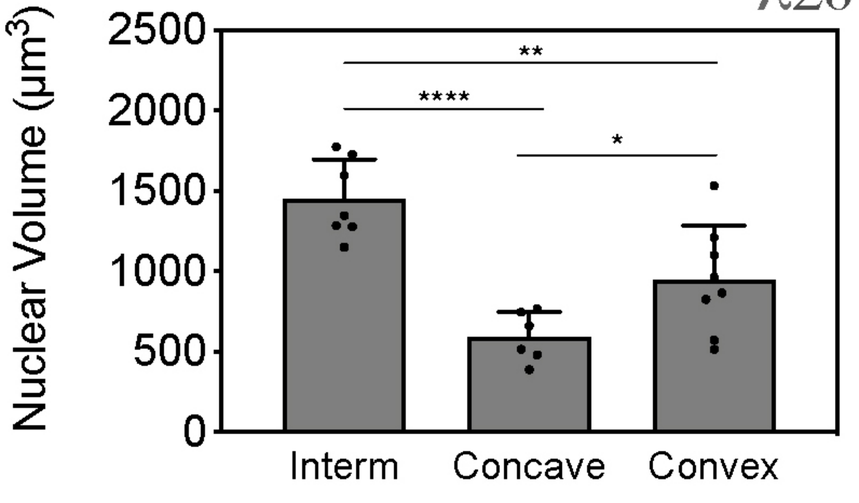

E

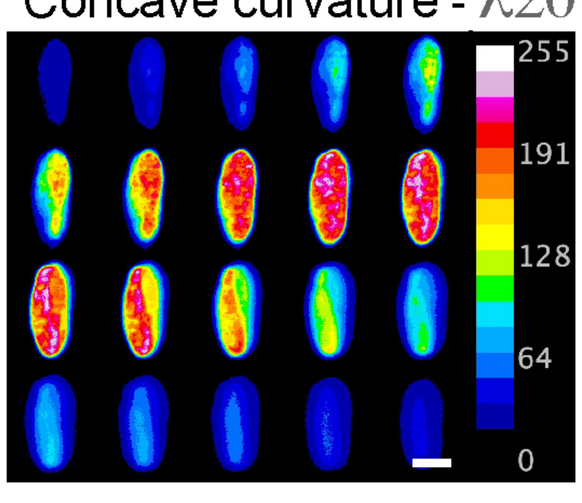

G

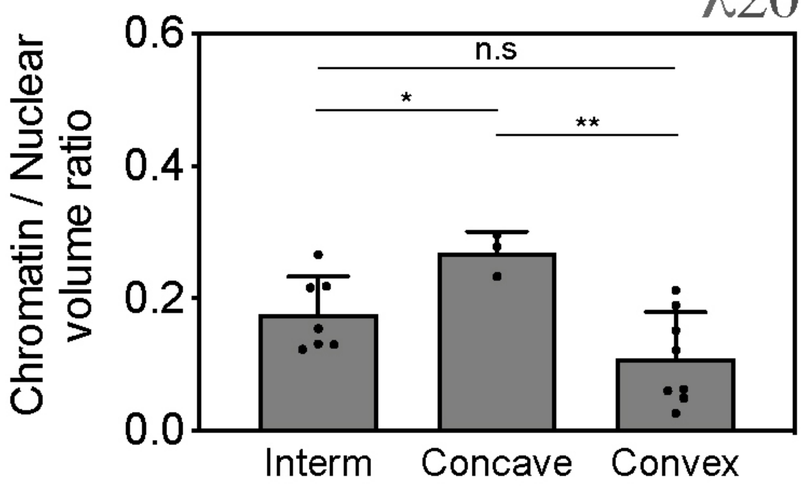

D

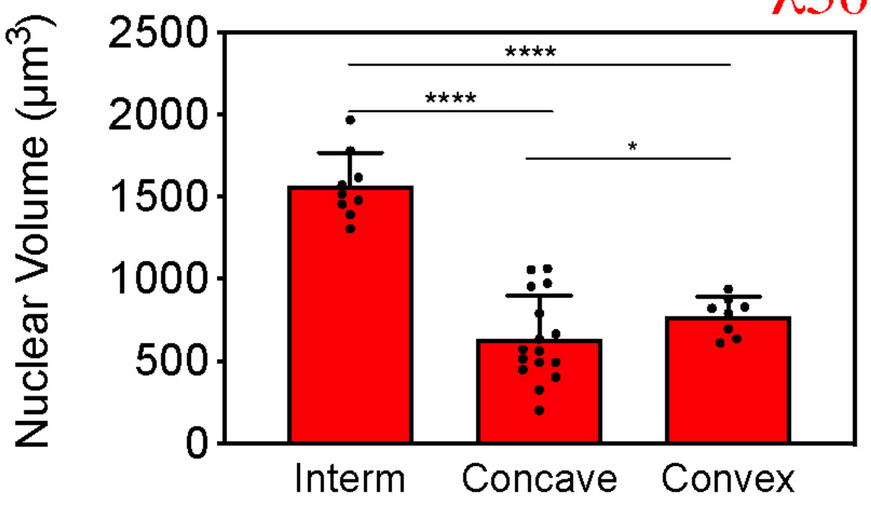

F

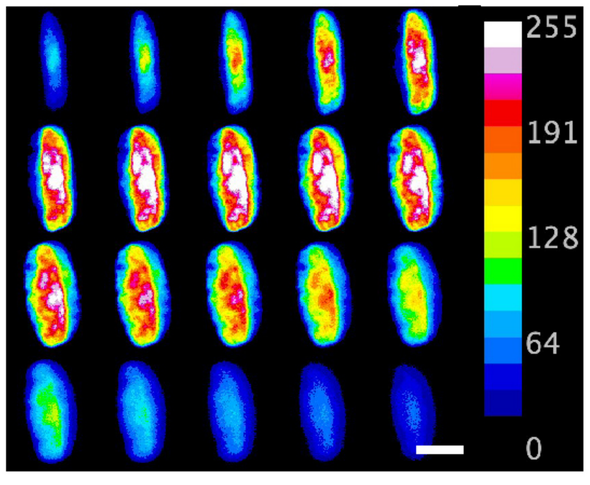

H

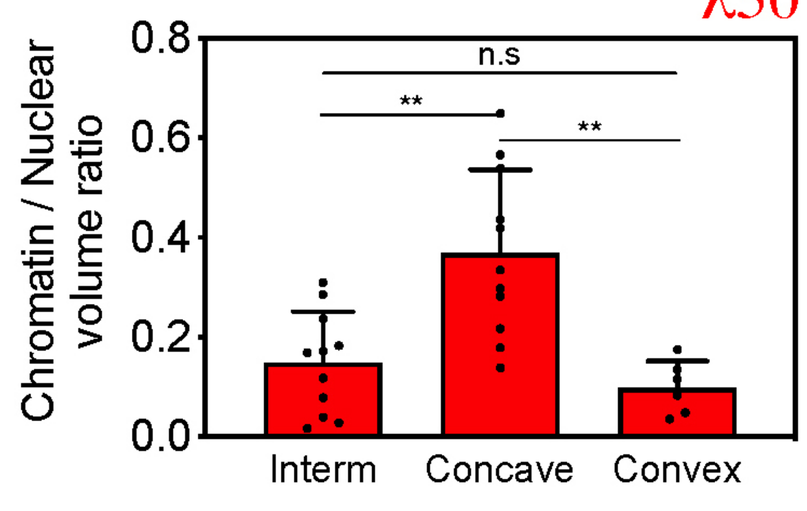

I

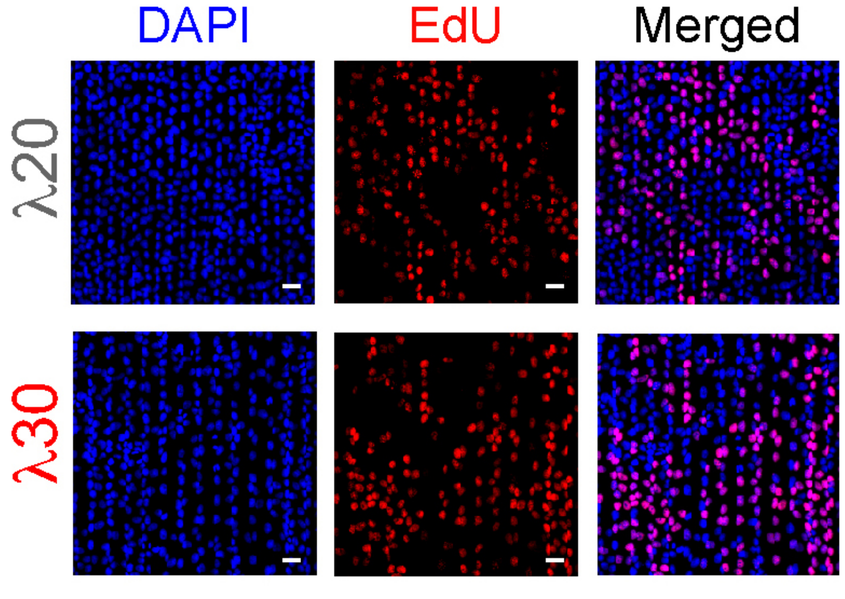

J

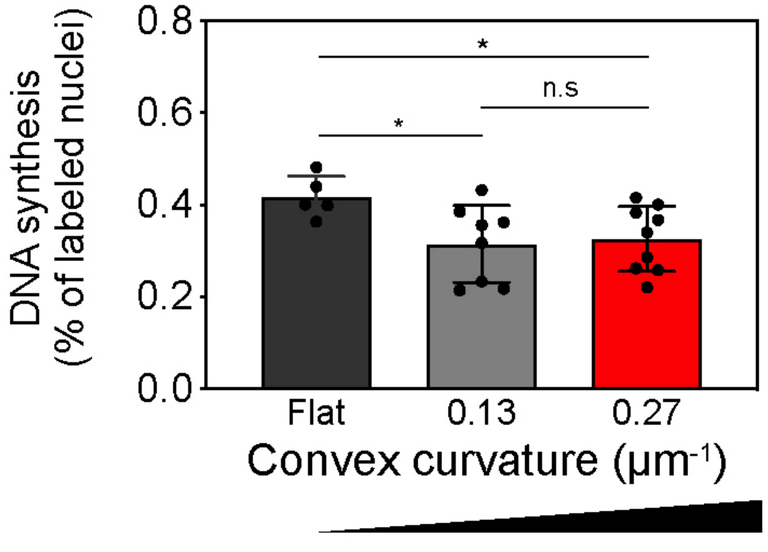

K